

École polytechnique de Louvain

Main title of the master thesis (possibly split on several lines)

Optional subtitle

Author: **Michele CERRA**
Supervisor: **Benoît MACQ**
Reader: **Alexandre BERGER**
Academic year 2022–2023
Master [120] in Computer Science and Engineering

Abstract

Acknowledgments

Contents

Abstract	1
Acknowledgments	1
Introduction	4
1 Theoretical background	6
1.1 Magnetic Resonance Imaging	6
1.1.1 Magnetic properties of nuclei	6
1.1.2 Radiofrequency pulse	8
1.1.3 Relaxation	9
1.1.4 Spin-echo sequence	11
1.1.5 Spatial coding	12
1.1.6 Artifacts	13
1.2 Diffusion-Weighted MRI	15
1.2.1 Pulse Gradient Spin Echo (PGSE)	15
1.2.2 Diffusion Tensor Imaging (DTI)	16
1.2.3 Tractography	18
1.3 DW-MRI Microstructural models	20
1.3.1 NODDI	20
1.3.2 DIAMOND	21
1.3.3 Microstructure fingerprinting	23
2 Epilepsy	26
2.1 Overview of Epilepsy	26
2.2 Vagus Nerve Stimulation	29
3 Methods	36
3.1 Data	36
3.1.1 Subjects	36
3.1.2 Data acquisition	36
3.2 Data preprocessing	37
3.3 Tractography	37
3.4 Microstructural analysis	37
3.5 Statistical analysis	37
4 Results	38

5 Discussion	39
5.1 Limitations	39
5.2 Applications	39
Conclusion and perspectives	39

Introduction

Chapter 1

Theoretical background

1.1 Magnetic Resonance Imaging

1.1.1 Magnetic properties of nuclei

Biological organisms and tissues are naturally abundant of *Hydrogen* atoms, mostly in water and fats. Thanks to the magnetic properties of Hydrogen atoms it is possible to build anatomical images of the human body.

From a classical point of view an atomic nucleus can be assumed as sphere rotating around its axis, as shown in Figure 1.1a. This rotation is called spin and it is a fundamental property of nucleus. The *spin* is the intrinsic angular momentum of the nucleus and can be an integer or a half-integer depending of the mass number¹ and the atomic number². In the particular case of the Hydrogen it is present only a proton and the spin can take only the values $1/2$ and $-1/2$. [1]

Since the nucleus is a charged particle, a rotation of it creates a magnetic field. From this point of view the particle behaves like a small magnetic dipole, as shown in Figure 1.1a: $\vec{\mu} = i\mathbf{S}$ where $\vec{\mu}$ is the intrinsic magnetic momentum that is aligned on its spin \mathbf{S} .

¹Mass number: number of protons and neutrons

²Atomic number: number of protons

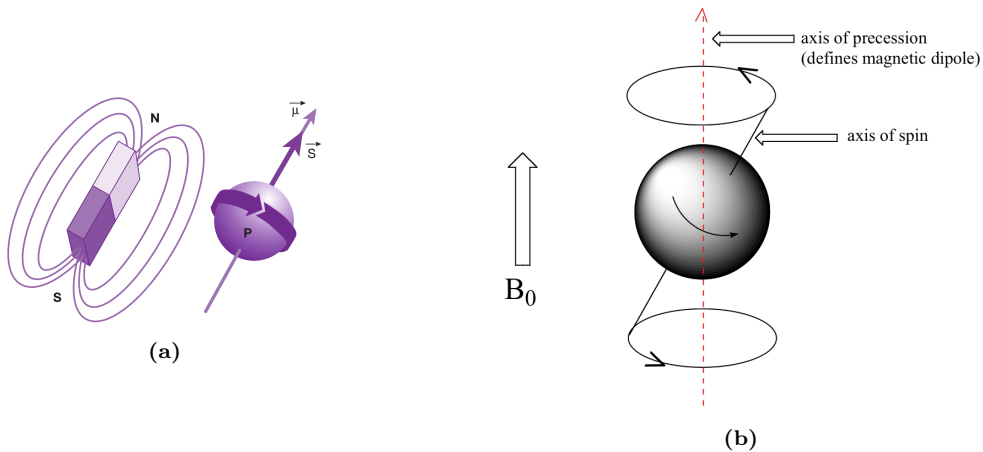


Figure 1.1: (a) Representation of the spin and the magnetic moment. [2], (b) Precessional motion of a proton spin in an applied magnetic field. [3]

Normally orientation of $\vec{\mu}$ is completely random due to thermal random motion, therefore the sum of the magnetic fields is null ($\sum_i \mu_i = 0$).

In a magnetic dipole, when an external magnetic field \mathbf{B}_0 is applied, the individual orientation can take two possible orientations: *parallel* or *anti-parallel*. This phenomena in the particles is different, since the particle is rotating, the external magnetic field creates a *precession* around \mathbf{B}_0 like a spinning top, as shown in Figure 1.1b: $\boldsymbol{\Gamma} = \vec{\mu} \times \mathbf{B}_0$ where $\boldsymbol{\Gamma}$ is the *torque*. The axis rotates around the area of a "cone", with an angular speed proportional to the applied field following the *Larmor's Law*:

$$f_0 = \frac{\gamma}{2\pi} B_0 \quad (1.1)$$

γ is the gyromagnetic ratio and it is a characteristic of the nucleus. The frequency of precession is called *Larmor frequency*.

From a global point of view, the populations of protons moments create a macroscopic magnetization, with the direction equal to the external field, as shown in Figure 1.2, defined by [1].

$$\mathbf{M} = \frac{1}{V} \sum_i \vec{\mu}_i \quad (1.2)$$

While the transversal magnetization in xy plane is null, since the components μ_{xy} rotate with different phases and overall they nullifying themselves, as shown on the left of Figure 1.2.

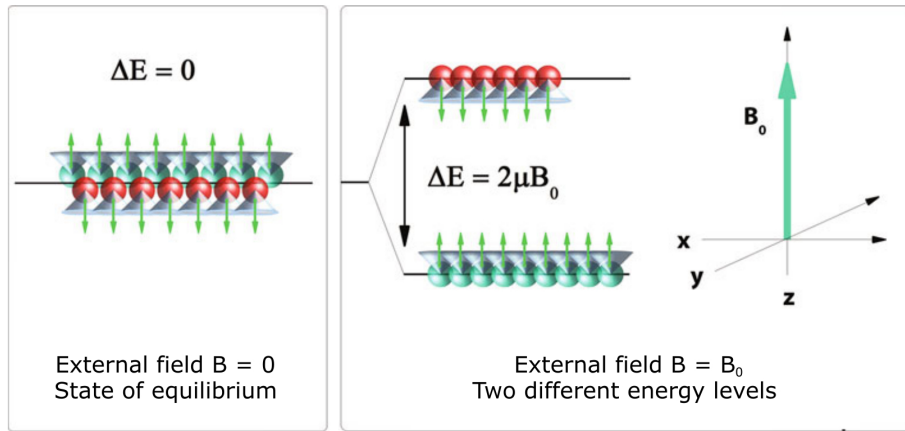


Figure 1.2: Separation of different energy levels after the application of the external field B_0 . The population of spins in the lower level is slightly more of the upper.[4] Translated.

In terms of energy, without the magnetic field, it doesn't exists any difference between the two orientations (parallel and anti-parallel), because them are equiprobable. With the application of the static magnetic field the anti-parallel orientation will have an higher energy ($N \downarrow$) than the parallel with lower energy ($N \uparrow$), since it has to be the opposite of the external field. The *occupation ratio* of the two energy levels is described by the *Boltzmann distribution*.

$$\frac{N_\uparrow}{N_\downarrow} = e^{-\frac{\Delta E}{kT}} \quad (1.3)$$

where k is the Boltzmann's constant and T is the absolute temperature in [K].

The energy of a magnetic dipole in a magnetic field \mathbf{B}_0 can be defined by:

$$E = -\vec{\mu} \cdot \mathbf{B}_0 = -\mu_z B_0 \Rightarrow$$

where $\mu_z = \gamma \frac{h}{2\pi} I$

$$\Rightarrow E_I = -\gamma \frac{h}{2\pi} I B_0$$

where h is the Planck's constant and I is the spin orientation for the Hydrogen.
Knowing that:

$$\Delta E = E_{-\frac{1}{2}} - E_{\frac{1}{2}} = h \frac{\gamma}{2\pi} B_0 = h f_0$$

we find that there are more spins in E_\uparrow (lower energy) state than E_\downarrow (higher energy) state, as shown in Figure 1.2.

The equilibrium macroscopic magnetization is non-zero and is defined by [1]:

$$M_0 = \frac{(\frac{\gamma}{2\pi})^2 h^2 \rho B_0 I (I + 1)}{3kT} \quad (1.4)$$

where ρ is the spin density³ and $I = 1/2$ for Hydrogen.

1.1.2 Radiofrequency pulse

Since the intensity of the macroscopic magnetization (M_0) is several orders of magnitude smaller than the main field (B_0), is impossible to measure it directly⁴.

The idea is to induce controlled oscillations of the spin system in order to generate a measurable signal as defined by [1]. If a RF pulse is applied at the Larmor frequency ($f_{RF} = f_0$) we observe a *condition of resonance* 1.3, and if the system resonates with the pulse it starts to absorb energy 1.4.

$$B_1(t) = 2B_1(t) \cos(2\pi f_{RF} t + \phi) \mathbf{1}_{xy} \quad (1.5)$$

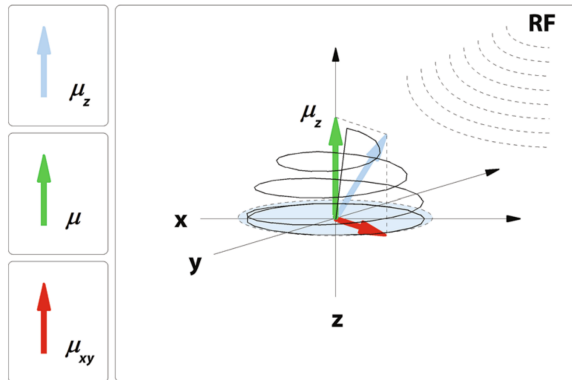


Figure 1.3: Trajectory of the magnetization vector. The vector describes a spiral trajectory by rotating at the Larmor frequency, tilting more and more, until it gets to rotate on the transverse plane. [4]

The *flip angle* from the initial direction of the magnetization is defined by [1]:

$$\theta = \gamma B_1 T_{RF}$$

where T_{RF} is the duration of the RF-pulse.

Now the magnetization vector can be represented with a longitudinal magnetization M_z and a transverse magnetization M_{xy} as in [1]:

$$\mathbf{M} = M_z \mathbf{1}_z + M_{xy} \mathbf{1}_{xy} \quad (1.6)$$

³Spin density: number of spins per unit volume

⁴Even if is impossible to measure directly the M_0 , it is proportional to the field, therefore an higher B_0 allows to generate higher signals with higher SNR and less acquisition times.

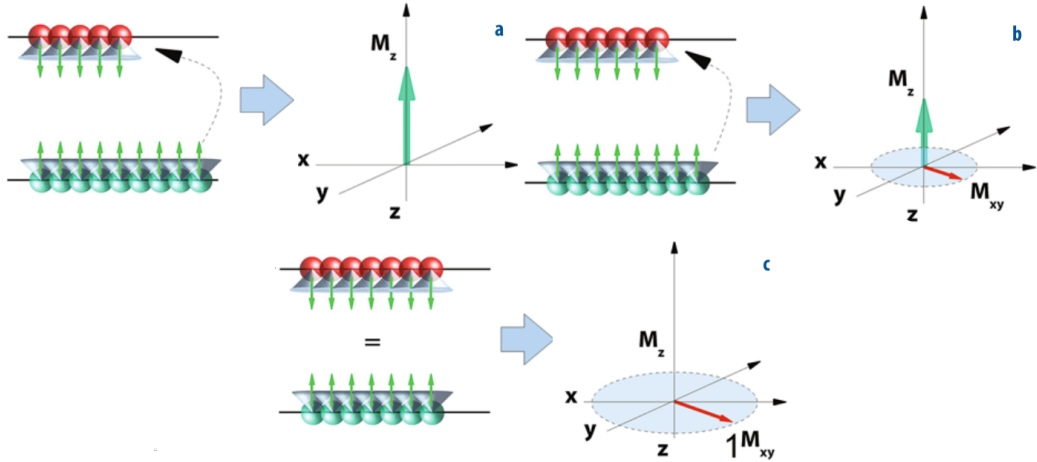


Figure 1.4: Effect of the RF impulse. (a) Initial situation; (b) System during the impulse; (c) System after 90 RF impulse. [4] Arranged.

1.1.3 Relaxation

After applying the RF-pulse tends to go back to the initial state, these phenomena are called *relaxation*.

$$M_z \rightarrow M_0$$

$$M_{xy} \rightarrow 0$$

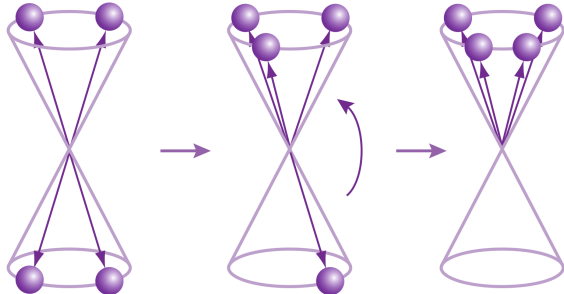


Figure 1.5: There is a progressively transition to the equilibrium from the high level to the lower lever of energy. [2]

The first is the *longitudinal relaxation* (*spin-lattice relaxation* or *T₁-relaxation*) in which the magnetization recovers to its original M_0 , because the energy state after the RF-pulse is unstable it will create a transition of spins from high energy to low energy, as shown in Figure 1.5. Can be mathematically described by [1]:

$$M_z(t) = M_0 + (M_z(0) - M_0)e^{-\frac{t}{T_1}} \quad (1.7)$$

where T_1 is the time needed to M_z to reach the 63% of the initial value M_0 , as shown in Figure 1.6.

In the T₁-weighted image the signals must depend on the T_1 relaxation. Therefore the time between the RF-pulses have to be brief, but sufficient to differentiate the different tissues, as shown in Figure 1.6. In these scans, the white matter is represented in light grey, the grey matter in a darker shade of grey and the fluids in black.

The second phenomenon is the *transverse relaxation* (*spin-spin relaxation* or *T₂-relaxation*) and it is characterized by a loss in coherence of the spin phases, as shown

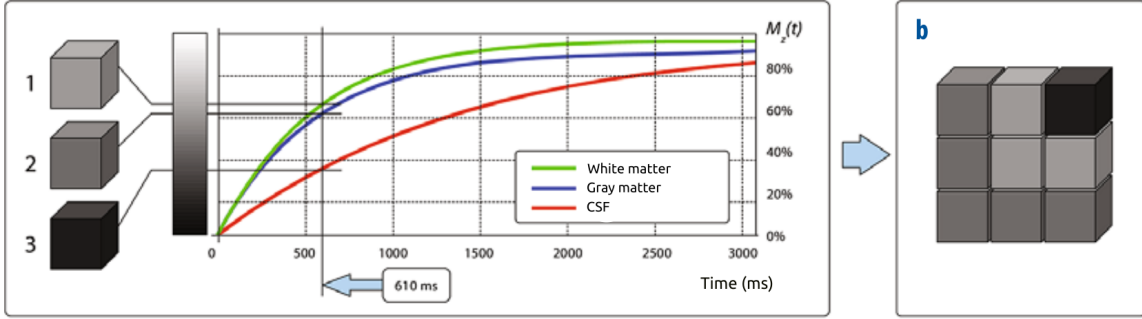


Figure 1.6: The T_1 relaxation time is different for type of tissues. [4] Translated.

in Figure 1.7. It can be written as in [1]:

$$M_{xy}(t) = M_{xy}(0)e^{-\frac{t}{T_2}} \quad (1.8)$$

where T_2 is the time needed to M_{xy} to reduce itself to 37% of the initial value 1.8.

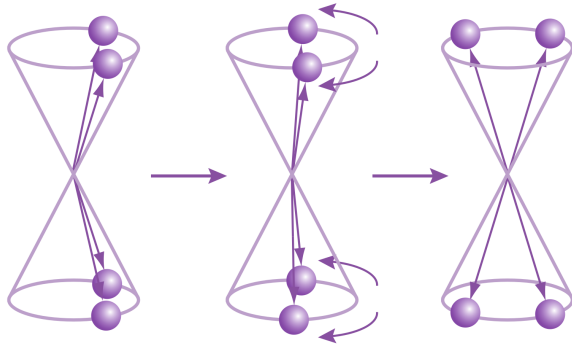


Figure 1.7: After the RF impulse there is a fast dephasing of the protons. The transversal magnetization M_{xy} decreases quickly. [2]

In the T_2 -weighted imaged the signals must depend only from the T_2 relaxation. Therefore is needed to wait that the T_1 relaxation effects are exhausted before reading the signal and send a new one. In these scans, the white matter is in dark grey, the grey matter is in light grey and the cerebrospinal fluid is in white, as shown in Figure 1.8.

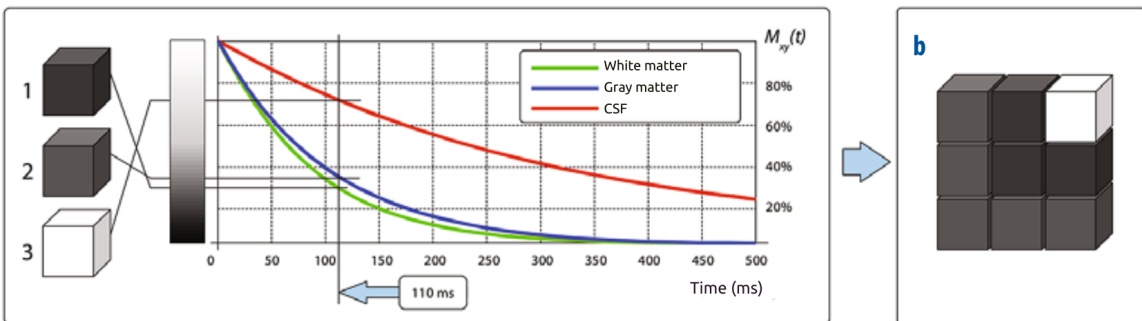


Figure 1.8: The T_2 relaxation time is different for type of tissues. [4] Translated.

In real conditions of an imperfect homogeneity of the field B_0 we see the *effective relaxation time*, define by [1]:

$$\frac{1}{T_{2*}} = \frac{1}{T_2} + \gamma \Delta B_0 \quad (1.9)$$

Where ΔB_0 are the inhomogeneities in the magnetic field.

1.1.4 Spin-echo sequence

To obtain images with different type of contrast is needed to control the time between RF-pulses and the time of between readings of the signal.

The first sequence utilized for clinical purpose is the *spin-echo*. It introduces two main parameters: *Echo time (TE)* and the *Repetition time (TR)*. The time between two 90° RF-pulses is defined ad *TR*, while the time between the RF-pulse and the first echo is defined as *TE*.

The strength of this sequence is the capacity of reading the T_2 -weighted signals and not the T_2^* 1.9.

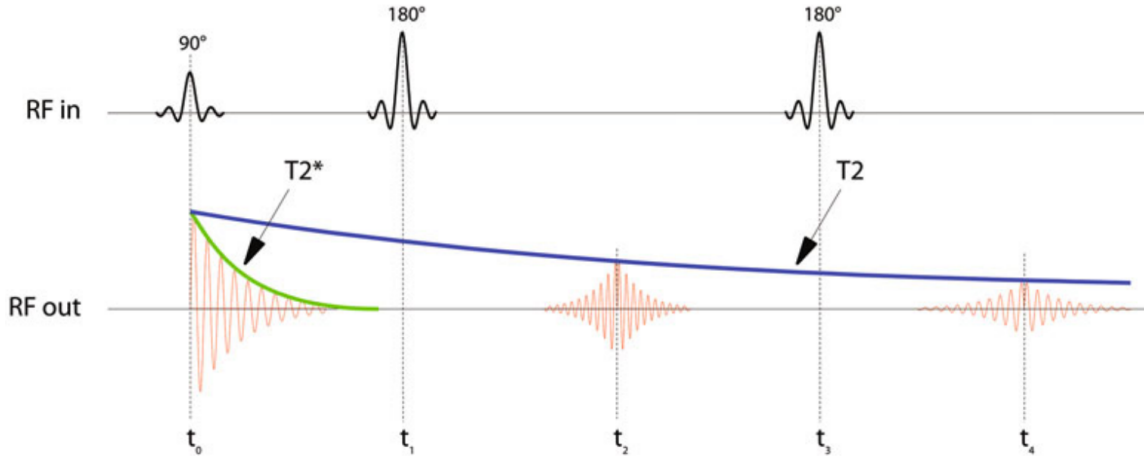


Figure 1.9: Recovering of the T_2 -weighted signals from the T_2^* through the Spin-echo sequence. The T_2 -weighted signals is created by interpolating the peaks of the spin echo signals. The time between t_0 and t_2 is defined ad *TE* [4]

The spin-echo sequence is composed of two type of RF-pulses: a 90° pulse and many 180° pulses. These last pulses have a double intensity and are called *echo impulses*. An echo impulse mirror all the spins of 180° , therefore the faster spins and the slower are inverted of position, creating the possibility that all the spins are refocused at time *TE*. [1]

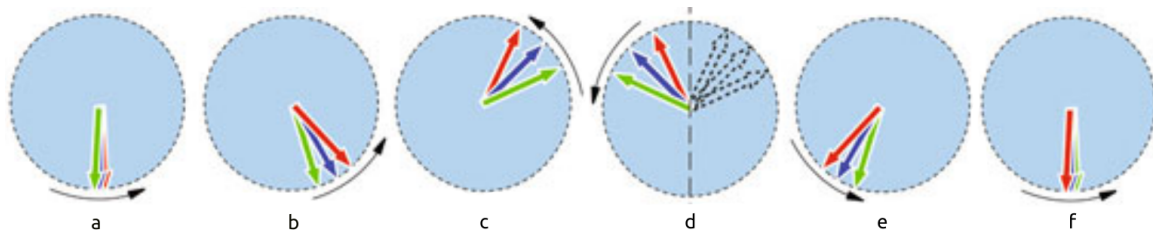


Figure 1.10: (a) After the end of the 90° RF impulse the protons are with the same phase. (b) The protons precession are different due to the inhomogeneities of the magnetic field. (c) The phases are completely different, there are some faster protons than others. (d) A 180° RF impulse move the proton position in a symmetric way in order to the slower protons are after the faster. (e) In the rotation the spins recover progressively the same phase. (f) At this time is generated a spin echo. [4] Arranged.

Contrast

By varying TE and TR , three types of contrast behavior can be obtained, as shown in Figure 1.11:

- $TE \ll T_2$ and $TR = T_1$: T_1 -contrast
- $TE = T_2$ and $TR \gg T_1$: T_2 -contrast
- $TE \ll T_2$ and $TR \gg T_1$: ρ -contrast (proton density)

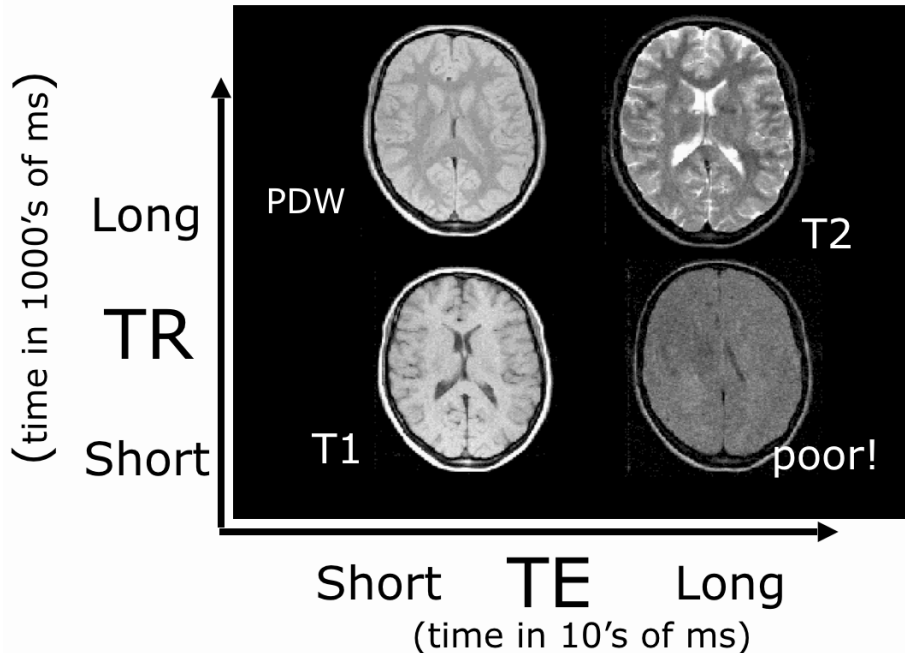


Figure 1.11: Matrix showing the different contrasts obtained with different TE and TR values. [5]

1.1.5 Spatial coding

To reconstruct the image it is needed selecting a definite volume of tissue called *voxel*⁵, three operations are needed to localize them in the tissue: selecting the layer (in the z-direction), selecting the column of the voxel (in the x-direction) and selecting the row (in the y-direction). These selections are done by linear variations of the magnetic field along a specific direction called *Gradient fields*. They can change the static magnetic field B_0 and thus change the precession frequency of protons.

To select a slice, it is applied a gradient along the z-direction, here the magnetic field change raising from a minimum to a maximum, and in the point in which the gradient is null the magnetic field is exactly B_0 . Therefore only the nuclei in the condition of resonance will generate a signal, see Figure 1.12.

Using a gradient on the x-direction (G_x) creates a signal that is the *sum of the associated signals with different frequencies*. This gradient is called *Gradient of*

⁵A voxel is the 3D expansion of a pixel

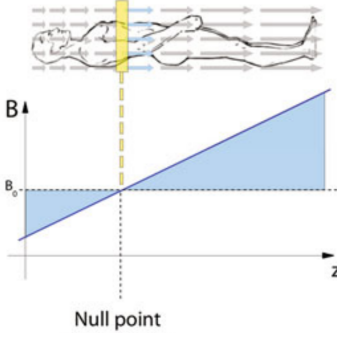


Figure 1.12: The effect of the gradient G_z is to resonate only the protons belonging to the slide in which the gradient is null (null point), only them have a field $B = B_0$ with a frequency equal to the Larmor frequency. [4]

frequency encoding, because the spins assume a precession frequency depending on the gradient. Successively, is applied a gradient along the y-direction (G_y), called *Gradient of phase encoding*, it change the spin phase depending on the gradient 1.13. In this way each element of the section is different from the other by phase or frequency.

The raw data from these signals are collected in matrices that represent the *k-space* in the frequency domain, in which G_y selects the row and G_x scans it and save it in the matrix. This sequence must be repeated n times for each line of the k-space to fill it, as shown in Figure 1.13. After, is applied the *Inverse Fourier transform* to retrieve the image in the spacial domain.

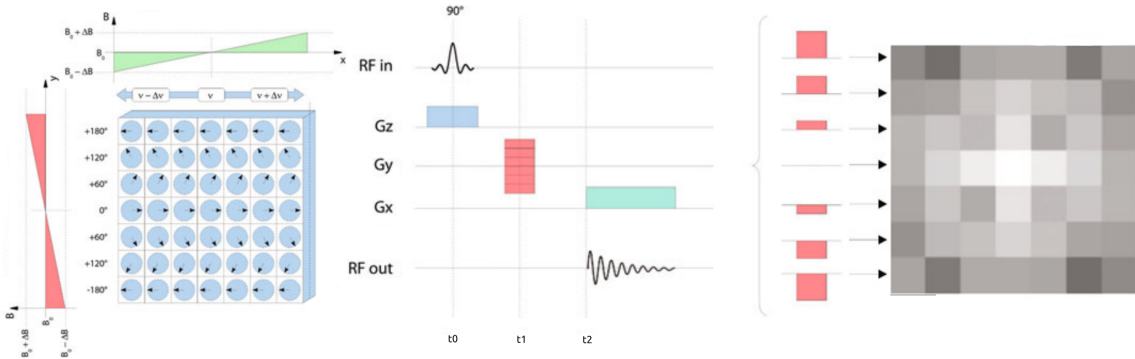


Figure 1.13: Gradients G_x and G_z , temporal diagram and k-space. [4] Arranged.

1.1.6 Artifacts

In MRI artifacts is everything that is represented in the image without any correlation with the real anatomy of the tissues analyzed.

Motion artifacts

The most common artifacts are the *movement artifacts* due to the involuntary movements of the patient. In general the movements can be divided in random and periodic movements. Random movements create a blurring of the image, while periodic movements create *ghost images*⁶. The first can be reduced using techniques that reduce the acquisition time. The periodic movements artifacts can be reduced through *gating*, a technique where the acquisition of the data is synchronized with the periodic movement of the tissue. [6]

⁶Ghost images: periodic copies of some structures of the image

Magnet susceptibility artifacts

The presence of ferromagnetic materials create local inhomogeneities in the magnetic field which result in distortion artifacts called *magnetic susceptibility artifacts*. The signals can change generating zone bright or dark with some distortions in the surrounding tissues. These artifacts can be reduced using spin-echo sequence instead of gradient-echo, and reducing the *TE*. [6]

Chemical shift

In the interface between tissues of different molecular characteristics can occur a *chemical shift*. It is a result of different resonance frequencies of adjacent tissues. Possible solutions are the reducing of the voxel dimension, increasing the bandwidth or using fat-suppressed imaging. [6]

Gibb's artifacts

Gibb's artifacts are due to the reconstruction from k-space, since it is performed through a finite sampling. In hedges of high-contrast the Fourier transform truncate some frequencies, for this they are also named *truncation artifacts*, creating the effect of fine parallel lines ("ringing") adjacent to such interfaces. Increasing the matrix size or applying smoothing filters can reduce the artifacts. [6]

Aliasing

Aliasing artifacts are visible when the tissue is outside the field-of-view (FOV), meaning that there was an under-sampling in the k-space. The only solution is to increase the size of the FOV or using techniques of foldover suppression. [6]

Eddy currents

The Faraday-Lenz Law of electromagnetism states that electrical currents (*Eddy currents*) are induced in nearby conductors by a changing magnetic field. Since MRI uses rapidly changing magnetic fields, eddy currents are always produced. The conductive material in which eddy currents are induced may be any metallic component of the MRI scanner and the patient as a whole. These latter may generate a distortion of the magnetic field. Several techniques are available to minimize te effects including image post-processing [7].

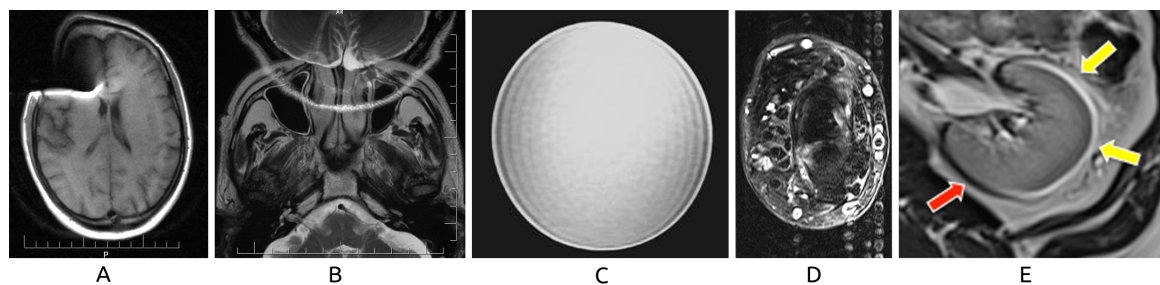


Figure 1.14: MRI artifacts: (A) Magnet susceptibility;; (B) Aliasing; (C) Gibb's ringing; (D) Chemical shift; (E) Chemical shift. [6] Arranged.

1.2 Diffusion-Weighted MRI

Sequences of *Diffusion-Weighted MRI* (DW-MRI) can provide motion-dependent contrast of water molecules in tissues, which can significantly alter in some brain diseases. These sequences are also known as *Diffusion Weighted Imaging* (DWI) or *diffusion MRI* (dMRI).

1.2.1 Pulse Gradient Spin Echo (PGSE)

The *Pulse Gradient Spin Echo* (PGSE) sequence is the main diffusion-weighted sequence used, it is composed of two magnetic gradients, before and after the 180° RF-pulse of the classic spin echo sequence. When the first diffusion gradient is applied, the water molecules are dephased, the second gradient, after the 180° RF pulse, will rephase the magnetization, as shown in Figure 1.15. The difference of gradient intensity which is subject to the water molecule is proportional to the distance traveled on the time between the two gradients and also the gradient intensity. Therefore, the protons that are moved faster will have a greater dephase.[4]

The intensity of a voxel can be described by the Stejskal-Tanner equation as defined in [8], in which the signal will be equal to the intensity of a T₂-weighted image, lowered by a quantity that depends on the diffusion of the molecules.

$$I = I_0 \cdot e^{-b_{PGSE} \cdot D} \quad (1.10)$$

where I is the intensity of received signal, I_0 is the intensity of base signal (T₂-weighted), b_{PGSE} is the factor of sensibility (parameters of PGSE sequence) and D is the coefficient of diffusivity (intrinsic characteristic of the tissue).

$$b_{PGSE} = (\gamma G \delta)^2 (\Delta - \frac{\delta}{3}) [s/mm^2] \quad (1.11)$$

where G is the diffusion gradient intensity, δ is the duration of the diffusion gradient and Δ is the time between the first diffusion and the second.

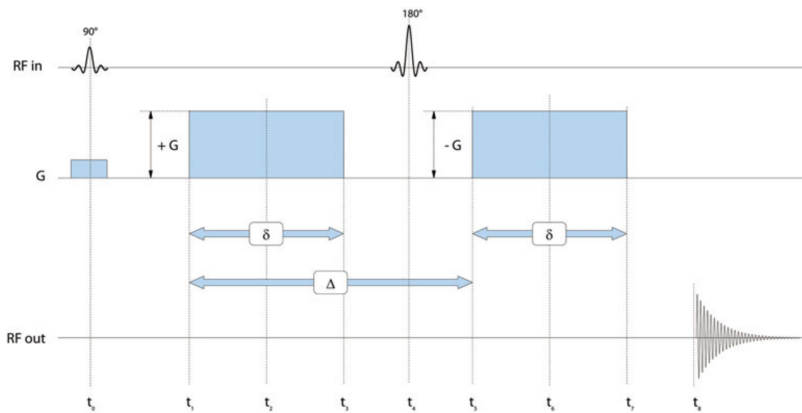


Figure 1.15: Between the two diffusion gradients is present the 180° RF pulse, therefore the second gradient is equal to the first one, because the spin was already flipped by the 180° RF pulse. [4]

The diffusion can be affected even to pressure, temperature and molecular interactions and the DW-MRI can not distinguish between these different causes. Furthermore, if the followed path during the diffusion is random rather than linear, the signal will be only a measure between the starting point and the end point. For these reasons

the D is not correct and should be replaced by a coefficient called *apparent diffusion coefficient (ADC)* [4].

$$I = I_0 \cdot e^{-b_{PGSE} \cdot ADC} \quad (1.12)$$

In the brain, the diffusivity of the water molecules is *anisotropic*, it is not equal in each direction of the space. For example the diffusion in the white matter will be higher along the direction of the axons rather than the perpendicular direction. While, if the diffusion does not have any preferential direction, such as in the CSF, the diffusion is called *isotropic*, see Figure 1.16. In this case the Stejskal-Tanner equation as defined in [8] becomes:

$$I = I_0 \cdot e^{-b_{PGSE} \cdot \hat{g}^T \mathbf{D} \hat{g}} \quad (1.13)$$

where \hat{g} is the gradient direction vector.

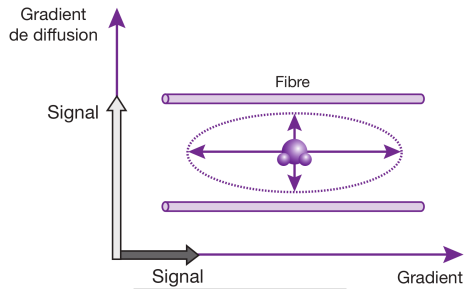


Figure 1.16: In the WM the diffusion of the water molecules is free along the axonal fibers, but it is reduced perpendicularly to the fibers. This is a case of Anisotropic diffusion. [2]

DWI collection involves setting a pre-determined number of gradient directions. That is, how many different angles within a 360-degree circle will water molecules be stimulated. For example, a DWI collection with 12 gradient directions will measure the diffusivity of water on every 30 degree angle, whereas a 32 gradient direction scan will measure every 11.25 degrees. [9]

1.2.2 Diffusion Tensor Imaging (DTI)

One of the most popular and widely used mathematical models to describe the primary orientation of white matter axonal path is called *diffusion tensor imaging*. This model was introduced in 1994 [10] and it consists of estimating an effective *diffusion tensor* (\mathbf{D}) within a voxel, which allows to represent its properties with a 3D ellipse. The diffusion tensor is described by a 3x3 symmetric tensor that uses 6 PGSE sequences, one for each different orientation of diffusion gradient, because $D_{yx} = D_{xy}$, $D_{zx} = D_{xz}$ and $D_{zy} = D_{yz}$.

$$\mathbf{D} = \begin{pmatrix} D_{xx} & D_{xy} & D_{xz} \\ D_{yx} & D_{yy} & D_{yz} \\ D_{zx} & D_{zy} & D_{zz} \end{pmatrix} \quad (1.14)$$

Using the eigendecomposition of \mathbf{D} are computed the eigenvectors and eigenvalues used to represent an ellipse on 3 orthogonal directions, as shown in Figure 1.17. The eigenvalues λ_i are the likelihoods of diffusion direction of a voxel. The largest eigenvalue(λ_1) is the principal direction of axons in that voxel.

$$\mathbf{D} = \mathbf{Q} \Lambda \mathbf{Q}^{-1}$$

$$\mathbf{\Lambda} = \begin{pmatrix} \lambda_1 & 0 & 0 \\ 0 & \lambda_2 & 0 \\ 0 & 0 & \lambda_3 \end{pmatrix} \quad (1.15)$$

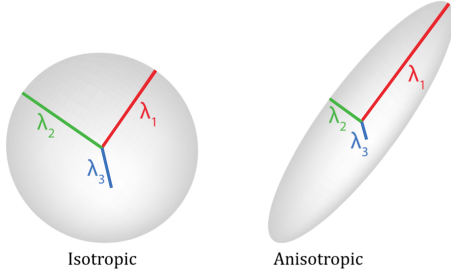


Figure 1.17: Isotropic and anisotropic tensor shapes, characterized by the eigenvalues of \mathbf{D} ($\lambda_1, \lambda_2, \lambda_3$). [11]

The result from the DW-MRI is difficult to visualize in a single image. In order to sintetize the information, the eigenvalues are used to compute some metrics that characterize each voxel. The most used are the *Mean Diffusivity (MD)* and the *Fractional Anisotropy (FA)* and they are computed by the *Trace* of the diffusion matrix as defined in [8].

$$MD = \frac{Tr(D)}{3} = \frac{\lambda_1 + \lambda_2 + \lambda_3}{3} \quad (1.16)$$

$$FA = \sqrt{\frac{3}{2} \frac{\sqrt{(\lambda_1 - MD)^2 + (\lambda_2 - MD)^2 + (\lambda_3 - MD)^2}}{\sqrt{\lambda_1^2 + \lambda_2^2 + \lambda_3^2}}} \quad (1.17)$$

The *MD* is proportional to the *Trace* and it quantify the amplitude of the ellipse, or how much a particle is freely to move. Therefore, the *MD* does not have any information about the directions, but on how much free water is contained into a voxel. The *FA* is a metric between 0 and 1 and it measures the degree of anisotropy in a voxel. More the diffusion directions are equal more the *FA* tends to 0. On the other and, an anisotropic diffusion will have a value of 1.

Other metrics are the *Axial Diffusivity (AxD)* and the *Radial Diffusivity (RD)*, defined in [8]. The Axial diffusivity is the diffusivity along the principal axis of the diffusion ellipsoid. While the Radial diffusivity is a measure used to express the diffusivity perpendicular to the principal direction of diffusion.

$$AxD = \lambda_1 \quad (1.18)$$

$$RD = \frac{\lambda_2 + \lambda_3}{2} \quad (1.19)$$

Both *FA* and *MD* can be represented on *diffusion direction maps*. The CSF will have an high *MD* since the water is free to move in all the directions, while the WM will have an high *FA* because oriented along a single direction. The image obtained from *FA* is called *FA map* and often they are displayed as *RGB FA maps*, in which colors are used to represent the principal direction of the diffusion (Red: left-right; Green: anterior-posterior; Blue: superior-inferior) .

Limitations of DTI

The main limitation of DTI model is that water molecules follow a Gaussian distribution. Therefore, only a bundle of fibers can be modeled inside each voxel, but in reality a complex organization of fibers is observed in every voxel. For example, a voxel containing two crossing fibers is modeled by a large diffusion tensor rather than two narrow tensors, as shown in Figure 1.18. Therefore in these voxel, the DTI model does not hold the assumption of a Gaussian distribution, and the resulting FA or MD metrics do not reflect the actual anatomical microstructure. [4]

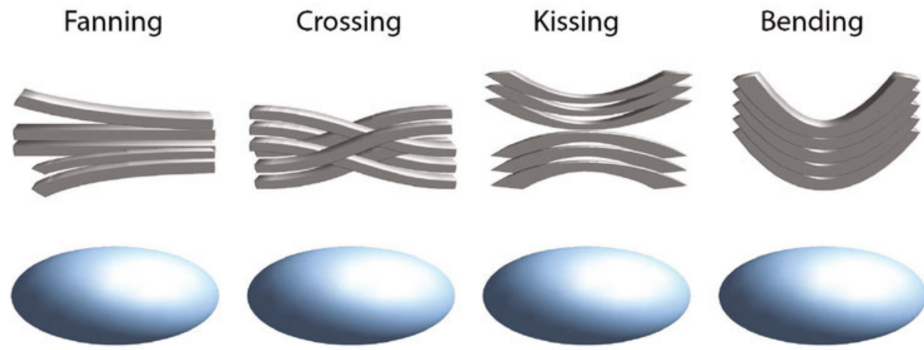


Figure 1.18: In the cases of *fanning*, *crossing*, *kissing*, *bending* the DTI model is not capable to distinguish the differences. [4]

1.2.3 Tractography

Tractography is a technique to estimate the pathways of the white matter fibers in the brain using data from DW-MRI. At the begin tractography was introduced by [12] using his proposed DTI model [10] [13]. But, DTI assumes that white matter fibers have a single orientation (tensor) within each voxel, which can lead to false trajectory results in regions with crossing fibers, as explained in 1.2.2 and Figure 1.18 [14]. To resolve these limitation more advanced algorithms as CSD (*Constrained Spherical Deconvolution*) [15] are used.

CSD estimate the *fiber orientation distribution* (FOD) from diffusion data. This distribution value provide information on other independent direction signal present within a voxel. In CSD model the signal $S(\theta, \phi)$ is assumed as convolution over the unit sphere between the fiber orientation density function (FOD) $F(\theta, \phi)$ and the response function $R(\theta)$, as defined in [16] and shown in Figure 1.19a:

$$S(\theta, \phi) = F(\theta, \phi) \circledast R(\theta) \quad (1.20)$$

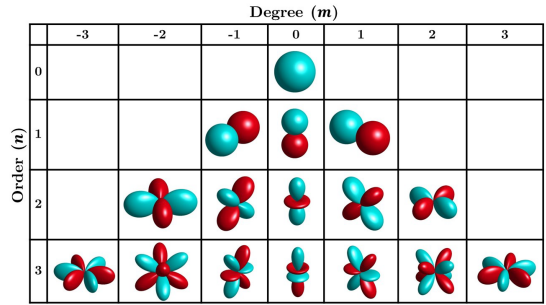
In order to estimate the FOD using CSD, it is first necessary to represent the FOD as a linear combination of *spherical harmonic basis functions* 1.19b. Then the fiber ODF $F(\theta, \phi)$ can be obtained by doing the *spherical deconvolution* [18].

CSD supports only data acquired form a single shell⁷, and can provide high quality

⁷In diffusion MRI, a "shell" refers to a set of diffusion-weighted images acquired using the same b-value or a range of b-values. Multi-shell diffusion MRI refers to the acquisition of diffusion-weighted images using multiple b-values(e.g., $b=0$, $b=1000$, 2000 , 3000 s/mm^2)

$$S(\theta, \phi) = R(\theta) \otimes F(\theta, \phi)$$

(a) 2D illustration of a voxel containing two fiber population. It can be expressed as a convolution over the unit sphere of an axially symmetric response function $R(\theta)$ with a fiber orientation density function $F(\theta, \phi)$. In this case $F(\theta, \phi) = \frac{1}{2}\delta(\theta_1, \phi_1) + \frac{1}{2}\delta(\theta_2, \phi_2)$. [16]



(b) Real parts of the spherical harmonics up to third order ($n = 0, 1, 2, 3$), for degree between $-3 \leq m \leq 3$, with lobes in cyan color indicating positive values and lobes in red color indicating negative values. [17]

fODF estimates in voxel containing WM only, in other cases the results may be unreliable and noisy. In [19] was developed a new model MSMT-CSD (*Multi-shell Multi-tissue CSD*), which takes in account also extra-cellular and other tissues for each voxel.

There are two different strategies used in fiber tractography: deterministic and probabilistic algorithms 1.20. Both of them get as input diffusion data or a FOD, and starting from seed points they follow a preferred diffusion direction. *Deterministic tractography* is a straightforward approach that involves tracking the dominant direction of diffusion at each voxel in the brain. However, deterministic tractography is sensitive to noise, crossing fibers (e.g. DTI model). *Probabilistic tractography* models the distribution of possible pathways rather than a single deterministic solution, the resulting tractography is based on a probability distribution of possible pathways. Probabilistic tractography can provide a more robust estimate of the tracts in the brain (e.g. MSMT-CSD model). [20]

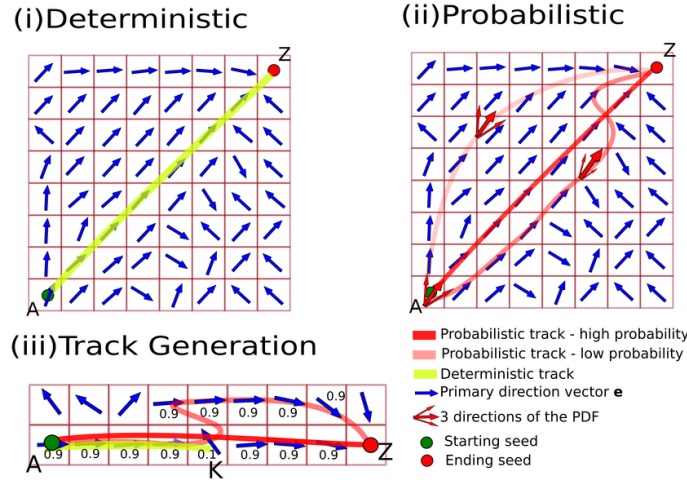


Figure 1.20: Basic example showing the difference between deterministic and probabilistic tracking models. [21]

1.3 DW-MRI Microstructural models

1.3.1 NODDI

Dendrites and axons, known collectively as neurites, are the cellular building blocks of the computational circuitry of the brain. Quantifying neurite morphology in terms of its density and orientation distribution provides a view between normal populations and populations with brain disorder. [22] Neurite Orientation Dispersion and Density Imaging (NODDI) is a three-compartment tissue model that models the microstructure complexity of dendrites and axons. Such indices of neurites provide more specific markers of brain tissue microstructure than DTI. [22]

NODDI distinguishes three types of microstructural environment: intra-cellular, extra-cellular and CSF compartments. Each gives to a separate normalized MR signal A_i combined as

$$A = (1 - \nu_{iso})(\nu_{ic}A_{ic} + (1 - \nu_{ic})A_{ec}) + \nu_{iso}A_{iso} \quad (1.21)$$

where A_{ic} , A_{ec} , A_{iso} and ν_{ic} , ν_{iso} are the normalized signal and volume fraction of intra-cellular, extra-cellular and CSF compartments respectively.

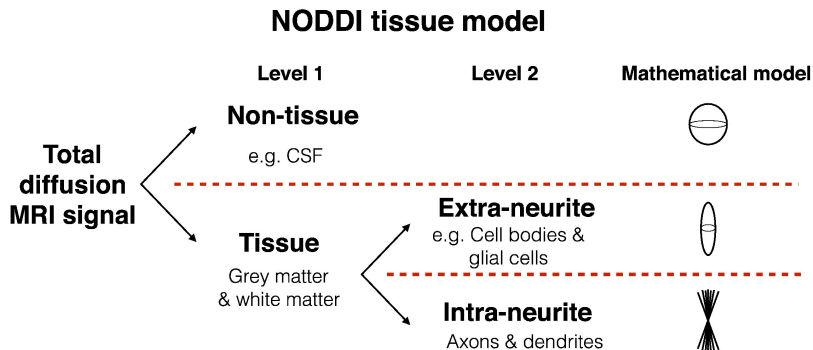


Figure 1.21: Different compartments modelled by NODDI. The non-tissue compartment is modelled by isotropic Gaussian diffusion. The intra-neurite compartment models the neurites as orientationally dispersed sticks, while the space around the neurites is prescribed an anisotropic diffusion model. [23]

The *intra-cellular* compartment refers to the space bounded by the membrane of neurites. This space is modeled by cylinders of zero radius (*stiks*), and their orientation distribution can range from highly parallel to highly dispersed. The orientation distribution function is modeled with a *Watson distribution*:

$$f(\mathbf{n}) = M\left(\frac{1}{2}, \frac{3}{2}, \kappa\right)^{-1} e^{\kappa(\mu \cdot \mathbf{n})^2} \quad (1.22)$$

where M is a confluent hypergeometric function, μ is the mean orientation, and κ is the concentration parameter that measures the extent of orientation dispersion about μ . The normalized signal, A_{ic} , is expressed as follows:

$$A_{ic} = \int_{\mathbb{S}^2} f(\mathbf{n}) e^{-bd_{||}(\mathbf{q} \cdot \mathbf{n})^2} d\mathbf{n} \quad (1.23)$$

where \mathbf{q} and b are the gradient direction and b-value of diffusion-weighting, $f(\mathbf{n})d\mathbf{n}$ gives the probability of finding stiks along orientation \mathbf{n} . $e^{-bd_{||}(\mathbf{q} \cdot \mathbf{n})^2}$ gives the signal

attenuation due to unhindered diffusion along a stick with intrinsic diffusivity d_{\parallel} and orientation \mathbf{n} .

The *extra-cellular* compartment refers to the space around the neurites which is occupied by various types of glial cells and additionally gray matter and cell bodies [22]. The diffusion motion is modeled by a Gaussian anisotropic distribution and the normalized signal is modeled with a tensor since the perpendicular dissusivities are taken in account:

$$\log A_{ec} = -b\mathbf{q}^T \left(\int_{S^2} f(\mathbf{n}) D(\mathbf{n}) d\mathbf{n} \right) \mathbf{q} \quad (1.24)$$

where $D(\mathbf{n})$ is the diffusion tensor with the principal diffusion direction \mathbf{n} , diffusion coefficients d_{\parallel} and d_{\perp} parallel and perpendicular to \mathbf{n} respectively. The parallel diffusivity (d_{\parallel}) is the same as the intrinsic free diffusivity of the intra-cellular compartment, while the perpendicular diffusivity (d_{\perp}) is set as $d_{\perp} = d_{\parallel}(1 - \nu_{ic})$.

The CSF compartment models the space occupied by cerebrospinal fluid and is model as isotropy Gaussian diffusion with diffusivity d_{iso} .

$$A_{ios} = e^{-bd_{iso}} \quad (1.25)$$

Model parameters

The complete set of parameters for the NODDI model is composed by: intra-cellular volume fraction (ν_{ic}) also called *Neurite Density Index (NDI)*, parallel diffusion coefficient (d_{\parallel}), concentration parameter of Watson distribution (κ), mean orientation of Watson distribution (μ), isotropic volume fraction (ν_{iso}), isotropic diffusivity (d_{iso}) [22]. The diffusivities are fixed to typical values⁸ and the remaining parameter are estimated. Furthermore, it is possible to compute the *Orientation Dispersion Index (ODI)* [24] which is a NODDI's summary statistic for quantifying angular variation of neurite orientation.

$$ODI = \frac{2}{\pi} \arctan\left(\frac{1}{\kappa}\right) \quad (1.26)$$

Limitations

NODDI focuses on explicitly modelling the fascicle dispersion with a Watson distribution of sticks in each voxel, but this assumption is inconsistent with the known tissue microstructure: fascicles with various microstructures have been observed in the brain. Furthermore it ignores the intra-axonal radial diffusivity and considers only a single fascicle compartment per voxel, while fascicles crossing with angle $> 40^\circ$ occurs in 60 – 90% of the voxels. NODDI can capture crossing fascicles as increased dispersion but cannot characterize each of them separately. [25]

1.3.2 DIAMOND

The signal arising from a voxel is composed by signals of multiple compartments. Model whose parameters reflect the tissue compartment present in each voxel are

⁸The diffusivities are fixed to respective typical values: $d_{\parallel} = 1.7 \times 10^{-3} \text{mm}^2 \text{s}^{-1}$ and $d_{iso} = 3 \times 10^{-3} \text{mm}^2 \text{s}^{-1}$

called *diffusion compartment models*, as shown in Figure 1.22a. The *Distribution of 3D Anisotropic Microstructural environments in Diffusion-compartment imaging* (DIAMOND) is an hybrid biophysical model of the tissues that combines multicompartiment and statiscal modelling to provide insight into each compartment in each voxel.[25]. It is inspired by the statistical framework of [26] but capable to characterize the three-dimensional anisotropy of diffusion observed in the brain and describe the spin packets' distribution of fascicles.

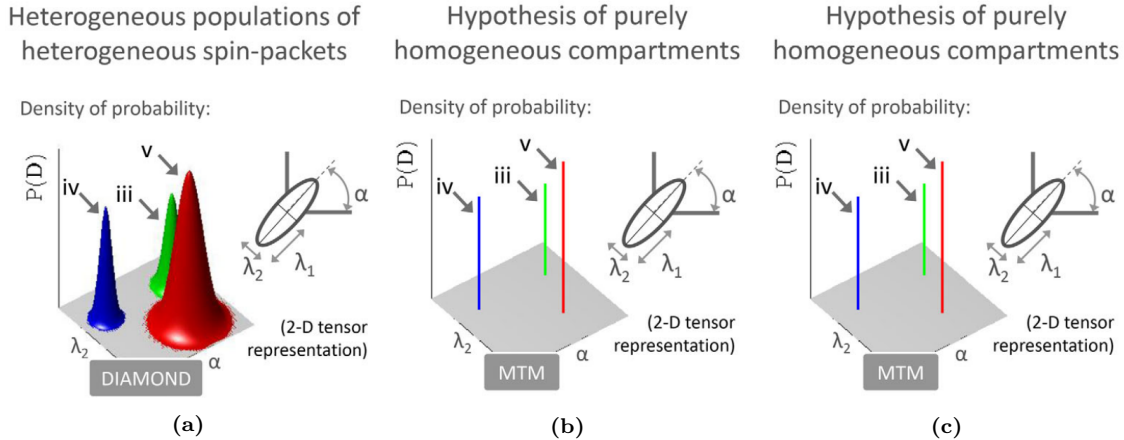


Figure 1.22: (a) Example of a voxel in which an isotropic (red) and two anisotropic (blue and green) compartments are mixed; (b) The corresponding probability density function of diffusivities is composed of a mixture of delta functions; (c) Peak-shaped distributions of diffusivities. [25]

DIAMOND requires the estimation of the number of tissue compartments in each voxel, which enables direct assesment of compartments-specific diffusion characteristic such as the compartment mean diffusivity (cMD), axial diffusivity (cAD) and radial diffusivity (cRD).

The fraction of spin packets described by a 3D diffusivity \mathbf{D} in the voxel is given by a *matrix-variate* distribution $P(\mathbf{D})$. Therefore, if a voxel consisted of exactly one *homogeneous* microstructural environment characterized by a tensor \mathbf{D}^0 , then $P(\mathbf{D})$ would be a delta function $P(\mathbf{D}) = \delta(\mathbf{D} - \mathbf{D}^0)$ and the model would be equivalent to DTI. While, if it consisted of several identifiable homogeneous microstructural environments, a mixture of delta functions would be used [25], as shown in Figure 1.22b. Then the DW signal S_k is modeled by:

$$S_k = S_0 \int_{\mathbf{D} \in Sym^+(3)} P(\mathbf{D}) \exp(-b_k \mathbf{g}_k^T \mathbf{D} \mathbf{g}_k) d\mathbf{D} \quad (1.27)$$

where $Sym^+(3)$ is the set of 3x3 SPD⁹ matrices, \mathbf{g}_k is the orientation of the diffusion gradient and b_k is the b-value of the sequence.

More realistically each microstructural environment contain some degree of *heterogeneity* and is best described by a *population of spin packets*. To reach this by modelling each population with a peak-shaped matrix-variate distribution centred in \mathbf{D}^0 , as shown in Figure 1.22c. DIAMOND uses a *matrix-variate Gamma* ($mv-\Gamma$)

⁹SPD: symmetric positive-definite matrices 3x3

distribution with *shape parameter* $\kappa > \frac{p-1}{2}$ and *scale parameter* $\Sigma \in Sym^+(3)$ [25].

$$P_{\kappa,\Gamma}(\mathbf{D}) = \frac{|\mathbf{D}|^{\kappa-(p+1)/2}}{|\Sigma|^{\kappa}\Gamma_p(\kappa)} \exp(-\text{trace}(\Sigma^{-1}\mathbf{D})) \quad (1.28)$$

where $|\cdot|$ is the matrix determinant and Γ_p is the multi-variate gamma function. It's expectation is $\mathbf{D}^0 = \kappa\Sigma$, and the shape parameter κ determines the concentration of the density around the mean value \mathbf{D}^0 . An heterogeneity index (*cHEI*) can be computed following the same transform as ODI in NODDI [22]: $cHEI(\kappa) = 2/\pi \arctan(1/\kappa)$.

Considering N_p populations each of them with a mv- Γ distribution $P_{\kappa_j,\Sigma_j}(\mathbf{D})$ with $j \in [1, \dots, N_p]$ the matrix-variate distribution is defined as [25]:

$$P(\mathbf{D}) = \sum_{j=1}^{N_p} f_j P_{\kappa_j,\Sigma_j}(\mathbf{D}) \quad (1.29)$$

where f_j are the occupation fractions and $\sum_{j=1}^{N_p} f_j = 1$.

Combining 1.27 and 1.29 and using the Laplace transformation, the following model is found [25]:

$$S_k = S_0 \sum_{j=1}^{N_p} f_j \mathcal{D}(\mathbf{D}_j^0, \kappa_j) \quad (1.30)$$

where $\mathcal{D}(\mathbf{D}^0, \kappa) = S_0(1 + \frac{b_k \mathbf{g}_k^T \mathbf{D}^0 \mathbf{g}_k}{\kappa})^{-\kappa}$.

Limitations

To summarise, DIAMOND focuses on capturing the distribution of 3D diffusivities arising from each tissue compartment (*model of the tissues*), and in contrast of the *model of the signal*, it requires the estimation of the number of tissue compartments (N_p) in each voxel, that is, the number of mv- Γ components. The estimation of N_p could be the only limitation of this model.

1.3.3 Microstructure fingerprinting

Microstructure fingerprinting is a model which leverages Monte Carlo simulation for the estimation of physically interpretable microstructural parameters, both in single and in crossing fascicles of axons in each voxel [27]. It is a multicompartment model as DIAMOND, each voxel is composed of different structures. Monte Carlo simulations of DW-MRI signals, or *fingerprints*, are pre-computed for a large collection of microstructural configurations. At every voxel, the microstructural parameters are estimated by optimizing a sparse combination of the fingerprints [27].

MF is based of the *superposition principle* of crossing fascicles, as shown in Figure 1.23, it assumes that the DW-MRI signal S of each voxel is composed by independent contributions of K fasciles of axons with different orientations \mathbf{u}_k occupying fractions ν_k of the physical volume and of a partial volume ν_{CSF} of cerebrospinal fluid [27]. S can be expressed as:

$$\begin{aligned} S &= M_0 \left[\sum_{k=1}^K \nu_k A_{fasc}(\Omega_k, \mathbf{T}_k, \mathbf{u}_k; \mathbf{g}) + \nu_{csf} A_{csf}(D_{csf}, \mathbf{T}_{csf}; \mathbf{g}) \right] \\ &= \sum_{k=1}^K w_k A_k + w_{csf} A_{csf} \end{aligned} \quad (1.31)$$

where M_0 is the initial transverse magnetization of the voxel, $A_k := A_{fasc}(\Omega_k, \mathbf{T}_k, \mathbf{u}_k; \mathbf{g})$ is the normalized DW-MRI signal of the k -th fascicle, modeled by a Monte Carlo simulation, that would arise from an environment composed of fascicles with parameters Ω_k and \mathbf{T}_k , and w_k is its weight defined as 1.32. Water is assumed to diffuse freely and isotropically with a scalar diffusivity D_{csf} .

$$w_k = M_0 \nu_k \iff \nu_k = \frac{w_k}{\sum_{k=1}^{K+1} w_k} \quad (1.32)$$

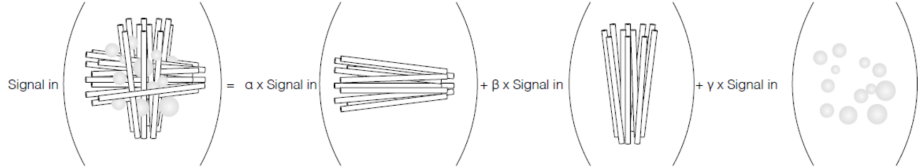


Figure 1.23: The total signal is the sum of the attenuation of each compartments weighted by the respective volume fractions. [28]

The dictionary is composed of DW-MRI signals (*fingerprints*) obtained by Monte Carlo simulations of the random walk of water molecules in environments defined by *hexagonal packing of impermeable cylinders* with different microstructural parameters Ω_k that represent the axons [27]. The fascicles are modeled by an axonal radius (r) and separation between the cylinders (s), see Figure 1.24.

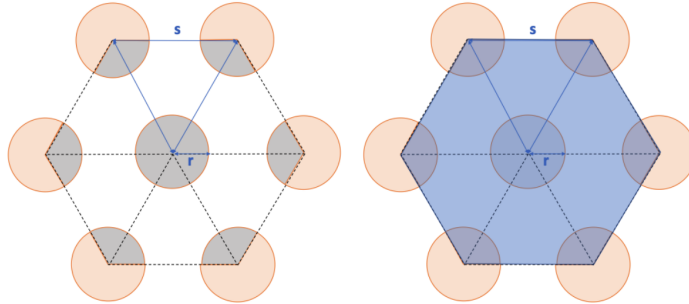


Figure 1.24: Representation of hexagonal packing of cylinders. At left a representation of the area of axons within the hexagon $A_{axons \subset hexagon}$, at the right the area of hexagon $A_{hexagon}$. [29]

Fascicle can be described by its intra-axonal volume fraction (or fiber volume fraction fvf), defined as ratio between the area of axons within the hexagon and the area of the hexagon 1.33, and by extra-axonal diffusivity D_{ex} .

$$fvf_{fasc} = \frac{A_{axons \subset hexagon}}{A_{hexagon}} = \frac{2\pi}{\sqrt{3}} \left(\frac{r}{s} \right)^2 \quad (1.33)$$

A canonical dictionary along the orientation $k = 0$, $C^0 = [A_1^0 \dots A_N^0] \in \mathbb{R}^{M \times N}$ is composed by concatenation of all the combinations of the possible fingerprints (fvf and D_{ex}). [30]

After pre-computing the canonical dictionary, the optimal combination of configurations is found at runtime. The runtime method consist in concatenating all the rotations of C_0 along each population and then solving a *sparse optimization problem* to find the best combination of fingerprint and orientation. The sparsity constraint ensure that only one fascicle is chosen out of all possible fascicle for a specific orientation

[31]. The sparsity constraint problem can be defined as:

$$(\hat{j}_1, \dots, \hat{j}_K) = \underset{1 \leq j_1, \dots, j_K \leq N}{\operatorname{argmin}} \underset{\mathbf{w} \geq 0}{\min} \left\| \mathbf{y} - \left[\mathbf{A}_{j_1}^1 | \dots | \mathbf{A}_{j_K}^K | \mathbf{A}_{csf} \right] \cdot \begin{bmatrix} w_1 \\ \vdots \\ w_K \\ w_{csf} \end{bmatrix} \right\| \quad (1.34)$$

where \mathbf{y} is the measured signal, and $\mathbf{A}_{j_k}^k = \{A_{fasc}(\Omega_{j_k}, \mathbf{T}_k, \mathbf{u}_k; \mathbf{g}_i(t))\}_{i=1}^M, 1 \leq j_k \leq N$ is the signal from of a fascicle with orientation u_k and microstructural parameters defined with index j . Finally, \hat{j}_k is the index of the optimal fingerprint in the k -th direction.

From the optimal fingerprints and the weights is possible to extract the metrics by:

$$\nu_k = \frac{w_k}{(w_k + w_{csf})}; \quad fvf_k = fvf_{\hat{j}_k}; \quad D_{ex,k} = D_{ex,\hat{j}_k}$$

Limitations

The use of the single scalars r and s to characterize the intra-axonal signal and the assumption on the impermeability of them is an overestimation of axons. Furthermore, the sparsity constraints do not allow mixtures of fingerprints to reconstruct the signal arising from a single fascicle of axons, this could be a limitation for fascicles with different microstructural properties in different sub-regions. [31]

Chapter 2

Epilepsy

2.1 Overview of Epilepsy

Epilepsy is a disorder of the brain characterized by a lasting predisposition to generate spontaneous epileptic seizures, and has a numerous neurobiological, cognitive, and psychosocial consequences [32]. Epilepsy affects over 50 million people worldwide, making it one of the most common neurological diseases globally [33]. Over 75% of those with active epilepsy are untreated [34].

Epilepsy incidence is bimodally distributed with two peaks: the first in the pediatric population less than 5 years old, and the second in people over the age of 50 years. The incidence is higher in low-income countries than high-income countries, thanks a contribution of poor hygiene, poor basic sanitation and higher risk of infection [35]. Regardless the geographical location, the prevalence of active epilepsy is usually between 4 and 12 per 1000, with a risk factor that varies with age [36].

The risk of death for a person with epilepsy is increased compared with the risk for the general population. Mortality in epilepsy can be divided into direct (eg, status epilepticus, injuries, SUDEP [37]) or indirect (eg, suicide, drowning) disease-related death [38].

SUDEP (Sudden Unexpected Death in Epilepsy) is one of the causes of epilepsy-related death, it refers to a death in a patient with epilepsy that is not due to trauma, drowning, status epilepticus, or other known causes but for which there is often evidence of an associated seizure [39]. The exact cause of SUDEP is not well understood, but it is thought to be related to abnormalities in the electrical activity of the brain during seizures, which can affect the heart and breathing [40]. SUDEP is most commonly seen in people with uncontrolled seizures, particularly those with generalized tonic-clonic seizures [40].

Epilepsy rarely stands alone and the presence of comorbidities is the norm: more than 50% of people with epilepsy have one or several additional medical problems [35]. These comorbidities not only include psychiatric conditions (e.g. depression, anxiety disorder, psychosis, autism spectrum disorder, dementia), but even somatic conditions (e.g. type 1 diabetes, arthritis, digestive tract ulcers) [41].

Definitions

Epilepsy

The given definition of Epilepsy is usually practically applied as having two unprovoked seizures occurring more than 24h apart. But the International League Against Epilepsy (ILAE) proposed that epilepsy be considered to be a disease of the brain by any of the following conditions: [32]

- At least two unprovoked seizures occurring more than 24h apart;
- A single unprovoked seizure if recurrence risk is high ($>60\%$ over the next 10 years);
- Diagnosis of an epilepsy syndrome.

Seizure

An epileptic seizure is the clinical manifestation of an abnormal, excessive, purposeless and synchronized electrical discharge in the neurons, that may lead to involuntary movement that may involve a part of the body (partial) or the entire body (generalized) [33]. Another type of generalized seizure is the absence seizure which is accompanied by loss of consciousness with periods of blanking out or staring into space for a few seconds [42].

Pathophysiology

A seizure can be conceptualized as occurring when there is a distortion of the normal balance between excitation and inhibition within a neural network [43].

In focal epilepsies, focal functional disruption results in seizures beginning in a localized fashion in one hemisphere, commonly limbic or neocortical, which then spread by recruitment of other brain areas. The site of the focus and the speed and extent of spread determine the clinical manifestation of the seizure [44, 45]. For generalized epilepsies, epileptogenic networks are widely distributed, involving thalamocortical structures bilaterally [45].

The imbalance between excitation and inhibition resulting in epileptogenic networks is not necessarily only an increase of excitation or a loss of inhibition; an aberrant increase in inhibition can also be pro-epileptogenic in some circumstances, such as absence seizures [46] or limbic epilepsies in the immature brain. [47]

Types of epilepsy

Classification is made at three levels: seizure type, epilepsy type, and epilepsy syndromes. [45]

Seizure type

Seizures are first classified by onset as either focal, generalized or unknown as shown in Figure 2.1.

- Focal Onset: Usually limited to a specific region of the brain, called the focus. Level of awareness subdivides focal seizure in those with retained awareness and impaired awareness. Retained awareness means that the person is aware of self and environment during the seizure, even if immobile. In addition, focal seizures are sub-grouped as those with motor and non-motor manifestation.
- Generalized Onset: Affects most or all of the brain. Typically congenital and occurs simultaneously in both hemispheres of the brain. They are almost always accompanied by impaired awareness. Generalized seizures are divided into motor and non-motor (absence) seizures.
- Unknown: It is the case in which the onset is missed or obscured.

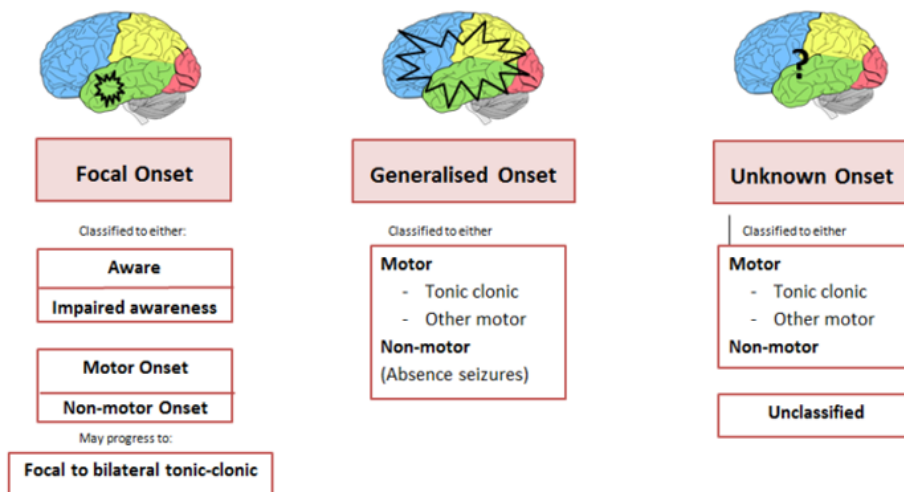


Figure 2.1: The International League Against Epilepsy.[48]

Epilepsy type

Epilepsies are divided into: focal, generalized, combined generalized and focal, and unknown as shown in Figure 2.2. The category combined epilepsy is used for those presenting both seizure types.

Causes of epilepsy

Each possible type of the classification can have different causes as shown in 2.2 : structural, genetic, infectious, metabolic, immune and unknown. Established acquired causes include serious brain trauma, stroke, tumours, and brain problems resulting from a previous infection. [35, 45]

Treatments

For most of the people with epilepsy Antiepileptic Drug(AEDs) constitute the first line treatment. However, it has been reported that AEDs are effective in only 60-70% of individuals, a percentage that is further reduced in low-income countries. [44].

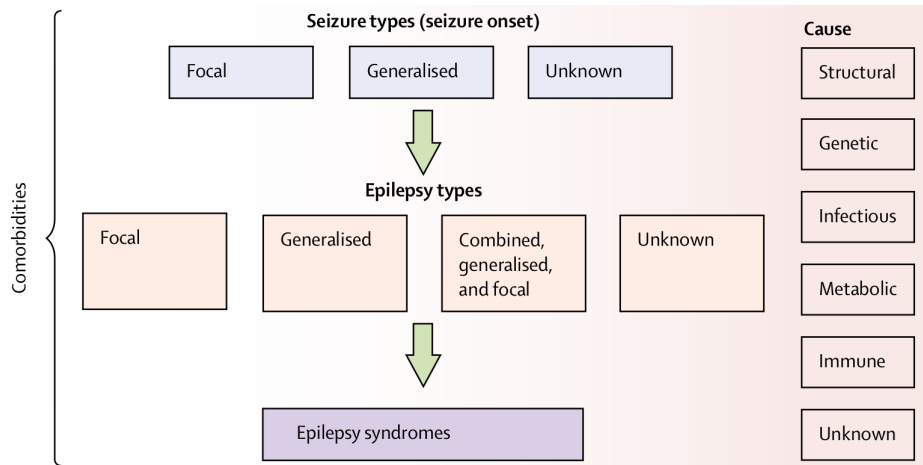


Figure 2.2: The International League Against Epilepsy.[35, 45]

Up to a third of all individuals with epilepsy are refractory to AEDs [49]. Drug-resistant epilepsy is assumed after the "failure of adequate trials of two tolerated, appropriately chosen and used at correct dosage antiseizure drug schedules to achieve sustained seizure freedom" [50]. In those cases alternative non-pharmacological treatments including surgery and neurostimulatory interventions should be considered. When surgery is not possible because of the presence of multifocal or generalized epilepsy or whenever the epileptogenic focus lies in eloquent cortex that cannot be removed, neurostimulation techniques are palliative options [51].

Three neurostimulation devices are approved by the Food and Drug Administration (FDA) for the treatment of drug resistant epilepsy [52].

- VNS is a device placed under the skin and sends intermittent signals to the vagus nerve. It is not a brain surgery and is approved for the treatment of epilepsy when surgery is not possible. [53]
 - RNS is a device that can record seizure activity directly from the brain and delivers stimulation to stop seizures. RNS is implanted near the seizure focus on the skull. It delivers pulses only when detects abnormal activity in the seizure focus. [53]
 - DBS sends signals to brain electrodes to stop signals that trigger a seizure. The connected DBS electrodes are typically placed inside the thalamus, and the electrical pulses are delivered constantly or not. [53]

2.2 Vagus Nerve Stimulation

Vagus Nerve Stimulation (VNS) showed positive effects in multiple other medical conditions, including essential tremors, gastroparesis [54], chronic tinnitus, stroke, post-traumatic stress disorder [55], chronic pain, Parkinson's disease, eating disorders, multiple sclerosis, migraine and Alzheimer's disease [56, 57].

VNS was implanted first time in four epilepsy patients by Penry and Dean in 1988 [58]. After several large clinical studies, it was approved for seizures by the

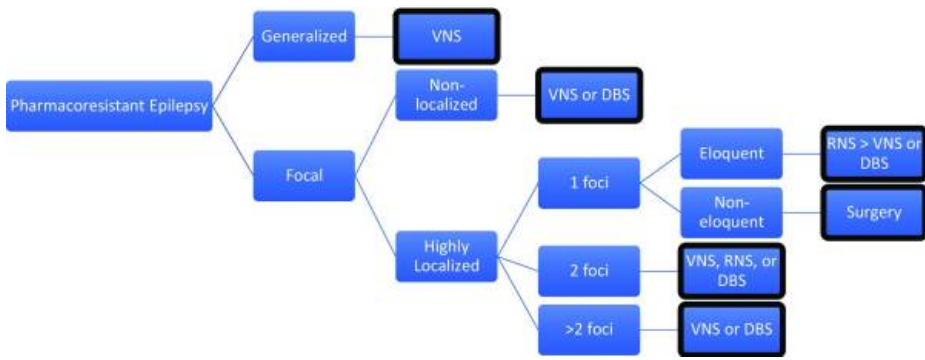


Figure 2.3: The following shows a general algorithm for efficacious device selection based on mechanism of action and focality. Other considerations (side effects, device features, and patient preferences) also drive device selection but are not captured in this flowchart. [52]

European Community in 1994 and FDA in 1997. Clinical trials demonstrate that 24 to 48 months after the implantation of the device, 60% of patients were considered as responders and 8% of implanted patients became seizure free [59]. Responders to VNS will be defined as those who experience 50% or greater reduction in seizure frequency after VNS [60]. Although VNS is used in clinical practice the exact mechanistic of its effect in modulating seizures remain poorly understood.

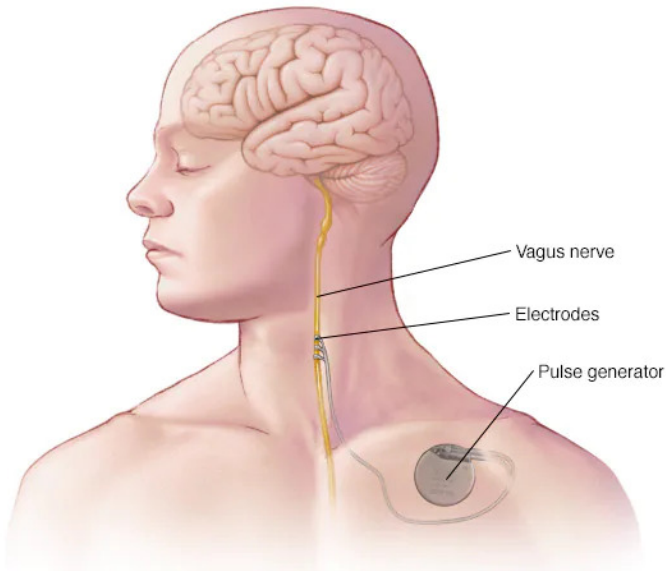
VNS consists of a device implanted in the upper left thoracic region with a helical electrode placed around the left cervical nerve, which delivers intermittent electrical impulses to activate the vagus nerve 2.4. Studies in the dog show that right-sided VNS results in a greater degree of bradycardia as compared to the left-sided VNS, because right vagus nerve innervates more densely in the heart [61]. Because on those studies VNS is indicated for use only in stimulating the left vagus nerve.

Side effects of VNS are commonly limited to coughing and/or hoarseness of the voice. In a study, voice alternation was reported in 66% of patients on high stimulation and in 30% on low stimulation and cough was reported in 45% of patients. [62] To avoid cardiac side effects, a cuff electrode in most cases is implanted on the left vagal nerve.

Vagus Nerve Anatomy and Connections

The vagal nerve (VN) is the longest cranial nerve and exerts a wide range of effects on the body. It comprises two nerves, the left and right vagus nerves and comprises both sensory and motor fibers. The vagal nerve is a mixed nerve made up of 75% sensory(afferent) fibers responsible for the side effects observed (e.g. coughing, difficulties of swallowing, voice modification effects), and 25% efferent fibers which mainly send feedback from heart, lungs, stomach and upper bowel. [64].

The majority of vagus nerve fibers are comprised of afferents and project to the nucleus tractus solitarius (NTS), which in turn sends fibers to other brainstem nuclei important in modulating the activity of subcortical and cortical circuitry, as shown in Figure 2.5. This vagus afferent network (VagAN) is thought to be the neural substrate of VNS efficacy [65]. The NTS receives direct inputs from the VN and projects to others brainstem nuclei: the locus coeruleus (LC), dorsal raphe nucleus (DRN), and parabrachial nucleus (PBN) [66]. The functional importance of NTS connectivity in modulating seizure activity is further borne out by findings in rats



© MAYO FOUNDATION FOR MEDICAL EDUCATION AND RESEARCH. ALL RIGHTS RESERVED.

Figure 2.4: Components of the VNS system. [63]

that increased inhibitory gamma-aminobutyric acid (GABA) signaling or decreased excitatory glutamate signaling within the NST, reduces the susceptibility to chemically induced limbic motor seizures [67].

The LC is characterized by widely diffused projections to both subcortical and cortical structures. The projections of the LC are small unmyelinated fibers, forming a wide antero-posterior branching network to reach the raphe nuclei, the cerebellum, and almost all areas of the midbrain and forebrain regions. The LC is the main source of norepinephrine (NE) in the brain [69]. NE is a neurotransmitter that has been associated with the clinical effects of VNS by preventing seizure development and by inducing long-term plastic changes that could restore a normal function of the brain circuitry. Indeed, short bursts of VNS increase neuronal firing in the LC, leading to elevations in NE concentrations. [70]

Studies have demonstrated indirect projection of the LC to the DRN, which sends widespread projections to upper cortical regions. DRN appears to have a more delayed response to VNS [65].

Vagal afferents project to the PBN by way of both the NTS and LC. Cell bodies within the PBN send diffuse outputs to forebrain structures including the thalamus, insular cortex, amygdala, and hypothalamus. Moreover, PBN likely plays an important role in regulating thalamocortical circuitry that may be implicated in seizure generation. Specifically, PBN activates the intralaminar nuclei of the thalamus, which in turn relays sensory signals to widespread cortical areas. [65]

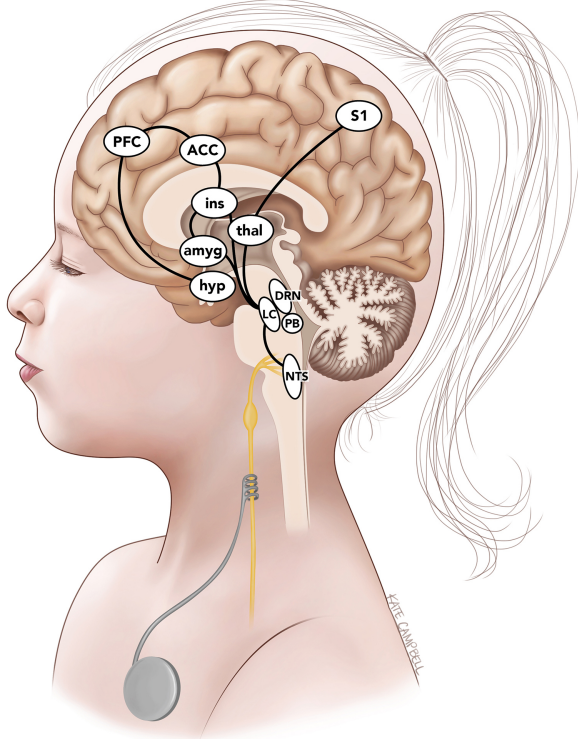


Figure 2.5: The vagus afferent network. Schematic diagram showing the important brain-stem centers and subcortical and cortical structures. [68, 65]

The Vagus Afferent Network

Structural and Functional connectivity

Structural connectivity and functional connectivity are two concepts that describe different aspects of brain organization. Structural connectivity refers to the anatomical organization of the brain by means of fiber tracts that connect different brain regions [71]. Functional connectivity refers to the statistical dependence or correlation of neural activity patterns between different brain regions [72]. Structural connectivity is often measured by diffusion magnetic resonance imaging (dMRI). Functional connectivity is often measured by electro-encephalography (EEG) or functional magnetic resonance imaging (fMRI)¹ [71].

The main difference between structural connectivity and functional connectivity is that structural connectivity reflects the physical architecture of the brain, while functional connectivity reflects the dynamic interactions of neural activity, as shown in Figure 2.6. Functional connectivity can emerge from direct or indirect structural connections, as well as from external inputs or intrinsic dynamics.

Functional connectivity results in VNS

Recently, thalamic activation measured by BOLD fMRI was associated with improved VNS treatment response in patients with seizures [74]. The importance of thalamo-cortical connections increased after a study that utilized resting-state functional MRI (rs-fMRI) data pre-VNS implantation and found an association of greater VNS efficacy with larger connectivity between the thalamus to the anterior cingulate cortex (ACC)

¹fMRI is a non invasive neuroimaging technique that detects the changes in blood oxygenation and flow that occur in response to neural activity

CONNECTIVITY

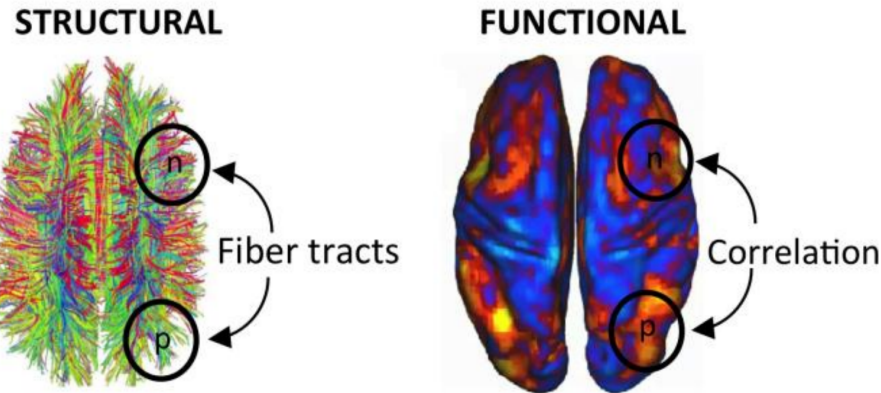


Figure 2.6: Differences between structural and functional connectivity [73].

and left insular cortex [60].

Functional connectivity in MEG² also supports the role of intrinsic thalamocortical connectivity in VNS responders, was found that a functional network is significantly more active in VNS responders [75, 76]. Specifically, fMRI studies in healthy individuals undergoing noninvasive VNS reported increased activity in the medial longitudinal fasciculus [77].

Structural connectivity results in VNS

Significantly greater FA was observed in VNS (lateralized to the left) responders particularly within anterior and retro lenticular limbs of the internal capsule, anterior, superior and posterior corona radiata, and posterior thalamic radiation [75].

In a study of 56 children done by [75] significantly greater FA (within the left size) was observed in VNS responders in the left internal capsule, external capsule, corona radiata, posterior thalamic radiation, fornix and stria terminalis, superior longitudinal fasciculus, inferior longitudinal fasciculus, and inferior front-occipital fasciculus. The mean FA value in these tracts was 0.352 (standard deviation SD = 0.048) in responders and 0.309 (SD = 0.064) in non responders. No significant voxels were observed in the right hemisphere. Furthermore, no statistically significant differences were observed in any other DTI parameters, including MD, radial diffusivity, and axial diffusivity. Healthy controls showed that the profile of responders was more closely related to healthy children than non responders. The mean FA value in significant tracts for matched controls was 0.377 (SD = 0.0274) in healthy controls. [75].

A study conducted on a 4-year-old boy with intractable epilepsy at 10 months after implantation of VNS showed increased FA in the right fimbria-fornix at the level of both cerebral peduncles. [78]

²Magnetoencephalography: is a functional neuroimaging technique that maps brain activity by recording magnetic fields produced by electrical currents occurring naturally in the brain, using very sensitive magnetometers.

Tracts of interest

Thalamocortical connections are believed to be an important substrate of VNS responsiveness because they modulate cortical excitability, rendering the brain less susceptible to seizures. The thalamus receives direct inputs from the NTS and PBN [79].

The limbic system is a collection of neuronal structures involved in controlling emotion, memory, behavior, and motivation. The fornix is the main efferent tract of the hippocampus projecting to the mammillary bodies, nucleus accumbens, septal nuclei, anterior thalamic nuclei and cingulate cortex. While, the stria terminalis forms the major input tract from the amygdala to the hypothalamus.

Association fibers link different cortical areas in the same hemisphere [80]. It is possible that they enable transmission of the modulatory stimulus to epileptogenic and/or symptomatogenic regions, which would be augmented by increased white matter microstructure in those tracts.

Thalamocortical connections

Fornix and Stria Terminalis

The *fornix* is apart of the limbic system and is a C-shaped bundle of nerve fibers that act as the major output tract of the hippocampus. [81] The *stria terminalis* is a fasciculus of fibers running along the lateral margin of the thalamus. It is the major output pathway of the amygdala. [82] Both fornix and stria terminalis are represented in Figure 2.7

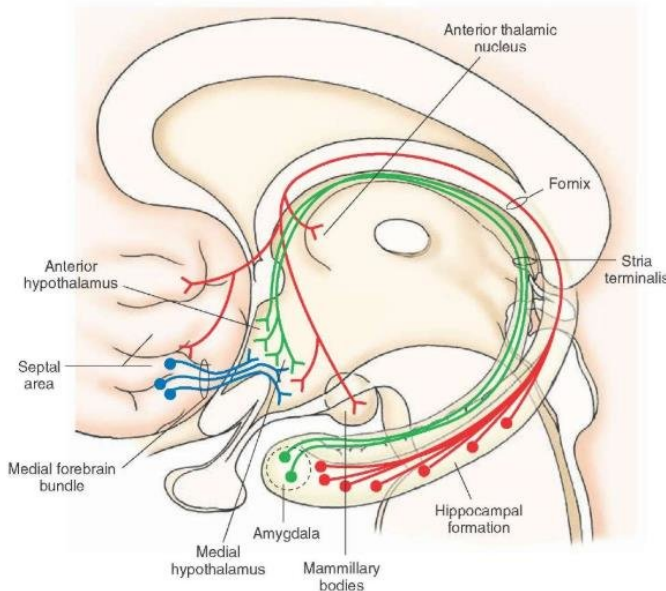


Figure 2.7: Illustration of anatomical structure and boundaries of stria terminalis and fornix. [83]

Association Fibers

The *superior longitudinal fasciculus* (SLF) is an association tract 2.8a in the brain that is composed of three separate components . The first (SLF I) is located in the white matter of the superior parietal and superior frontal lobes. The second, (SLF II)

occupies the central core of the white matter above the insula. While the last one, (SLF III) is situated in the white matter of the parietal and frontal opercula. [84]

The *inferior longitudinal fasciculus* is an associative white matter pathway that connects the occipital and temporal-occipital areas to the anterior temporal areas as shown in Figure 2.8b.

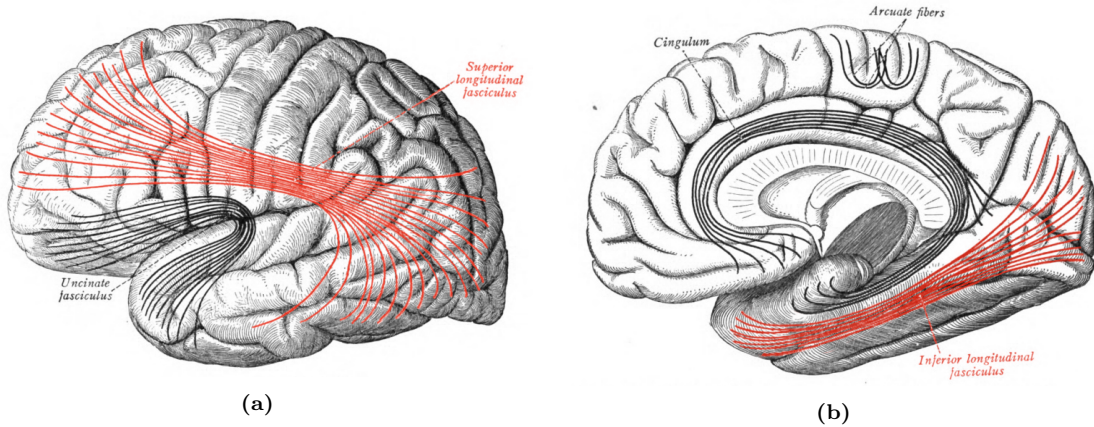


Figure 2.8: Representation of longitudinal fascicles: (a) Superior longitudinal fasciculus; (b) Inferior longitudinal fasciculus. [85]

Chapter 3

Methods

3.1 Data

3.1.1 Subjects

3.1.2 Data acquisition

The MRI acquisitions were realized following the *LivaNova guidelines*, requiring the neurostimulators to be turned off during the acquisitions. A trained neurologist used the programming system to set the output current of the device to 0 mA and turn off the sensing before that the patients entered the MRI acquisition room.

Imaging data were acquired using the *SIGNA™ Premier 3T MRI* system (GE Healthcare, Milwaukee, WI, USA), with a transmit-receive 48-channel head coil.

T1-anatomical images were acquired using a *Magnetization Prepared - RApid Gradient Echo* (MPRAGE) sequence with the following parameters: $TR = 2186ms$, $TE = 2.95ms$, $FA = 8^\circ$, $TI = 900ms$, bandwidth = $244.14Hz$, matrix size = 256×256 , 156 axial slices, imaging frequency = $127.77Hz$, voxel size = $1 \times 1 \times 1 mm^3$, acquisition time = 5:26 min.

Diffusion MRI data were acquired with a *Pulsed Gradient Spin Echo* (PGSE) sequence with the following parameters : $TR = 4837ms$, $TE = 80.5ms$ and flip angle = 90° . A multi-shell diffusion scheme was used and was composed of 64 gradients at $b = 1000$, and 32 gradients at $b = 2000$, 3000 and $5000 [s \cdot mm^{-2}]$, interleaved with 7 b0 images. The in-plane FOV was $220 \times 220 mm^2$ and the data contained 68 axial slices with a $2mm$ thickness (no inter-slice gap, $2mm$ isotropic voxels). A multi-slice excitation scheme was used during the acquisition with a hyperband slice factor of 3 to reduce the acquisition time. The total acquisition time was 13:33 min.

Anatomical files are composed of a NIfTI file (`.nii.gz`) 3.2 containing the measured signal and a JSON file (`.json`) regrouping the acquisition sequence parameters.

Figure 3.1: Anatomical volume slices of a T1 in the sagittal, frontal and axial views

Figure 3.2: Anatomical volume slices of a T2 in the sagittal, frontal and axial views

Diffusion files are composed of a NIfTI file and a JSON file plus two text files (`.bval`) and (`.bvec`) containing the b-values and the b-vectors.

Figure 3.3: Raw diffusion volume slices of a patient for different b-values

3.2 Data preprocessing

3.3 Tractography

3.4 Microstructural analysis

3.5 Statistical analysis

Chapter 4

Results

Chapter 5

Discussion

5.1 Limitations

5.2 Applications

Conclusion and perspectives

Bibliography

- [1] F. Peeters, “Medical imaging, chapter 4 : Magnetic resonance imaging.” LGBIO2050, UCL.
- [2] D. V. B. Kastler, *Comprendre l'IRM: Manuel d'auto-apprenissage*. Imagerie médicale DIAG-NOSTIC, 1988.
- [3] S. R. Kennepohl D., Farmer S., *Theory of Nuclear Magnetic Resonance (NMR)*, ch. 13. Mind-Touch, 2019.
- [4] M. C. O. Rampado, *Elementi di risonanza magnetica*. Springer, 2017.
- [5] Q. Sameer, “Magnetic resonance imaging (mri) in orthopaedics,” 2017. Last accessed 28 April 2023.
- [6] B. Y. Weerakkody Y., Murphy A., “Mri artifacts,” 2012. Available at <https://radiopaedia.org/articles/16585>.
- [7] A. D. Elster, “Eddy currents.” Available at <https://mriquestions.com/eddy-current-problems.html>.
- [8] S. S. Wim Van Hecke, Louise Emsell, *Diffusion Tensor Imaging, A Pratical Handbook*. Springer.
- [9] E. H. de Figueiredo, A. F. Borgonovi, and T. M. Doring, “Basic concepts of mr imaging, diffusion mr imaging, and diffusion tensor imaging,” *Magnetic Resonance Imaging Clinics*, vol. 19, no. 1, pp. 1–22, 2011.
- [10] P. J. Basser, J. Mattiello, and D. LeBihan, “Mr diffusion tensor spectroscopy and imaging,” *Biophysical journal*, vol. 66, no. 1, pp. 259–267, 1994.
- [11] D. Tromp, “The diffusion tensor, and its relation to fa, md, ad and rd,” 2015. Available at <https://www.diffusion-imaging.com/2015/10/what-is-diffusion-tensor.html>.
- [12] P. J. Basser, “Fiber-tractography via diffusion tensor mri (dt-mri),” in *Proceedings of the 6th Annual Meeting ISMRM, Sydney, Australia*, vol. 1226, 1998.
- [13] P. J. Basser and C. Pierpaoli, “Microstructural and physiological features of tissues elucidated by quantitative-diffusion-tensor mri,” *Journal of magnetic resonance*, vol. 213, no. 2, pp. 560–570, 2011.
- [14] P. J. Basser, S. Pajevic, C. Pierpaoli, J. Duda, and A. Aldroubi, “In vivo fiber tractography using dt-mri data,” *Magnetic resonance in medicine*, vol. 44, no. 4, pp. 625–632, 2000.
- [15] J.-D. Tournier, F. Calamante, and A. Connelly, “Robust determination of the fibre orientation distribution in diffusion mri: non-negativity constrained super-resolved spherical deconvolution,” *Neuroimage*, vol. 35, no. 4, pp. 1459–1472, 2007.
- [16] J.-D. Tournier, F. Calamante, D. G. Gadian, and A. Connelly, “Direct estimation of the fiber orientation density function from diffusion-weighted mri data using spherical deconvolution,” *Neuroimage*, vol. 23, no. 3, pp. 1176–1185, 2004.
- [17] N. Xiang and C. Landschoot, “Bayesian inference for acoustic direction of arrival analysis using spherical harmonics,” *Entropy*, vol. 21, no. 6, 2019.
- [18] D. M. Healy Jr, H. Hendriks, and P. T. Kim, “Spherical deconvolution,” *Journal of Multivariate Analysis*, vol. 67, no. 1, pp. 1–22, 1998.

- [19] B. Jeurissen, J.-D. Tournier, T. Dhollander, A. Connelly, and J. Sijbers, “Multi-tissue constrained spherical deconvolution for improved analysis of multi-shell diffusion mri data,” *NeuroImage*, vol. 103, pp. 411–426, 2014.
- [20] T. E. Behrens, H. J. Berg, S. Jbabdi, M. F. Rushworth, and M. W. Woolrich, “Probabilistic diffusion tractography with multiple fibre orientations: What can we gain?,” *neuroimage*, vol. 34, no. 1, pp. 144–155, 2007.
- [21] E. Garyfallidis, *Eleftherios Garyfallidis, "Towards an accurate brain tractography"*, PhD thesis, University of Cambridge, 2012. PhD thesis, 05 2012.
- [22] H. Zhang, T. Schneider, C. A. Wheeler-Kingshott, and D. C. Alexander, “Noddi: practical in vivo neurite orientation dispersion and density imaging of the human brain,” *Neuroimage*, vol. 61, no. 4, pp. 1000–1016, 2012.
- [23] M. Tariq, T. Schneider, D. C. Alexander, C. A. Gandini Wheeler-Kingshott, and H. Zhang, “Bingham–noddi: Mapping anisotropic orientation dispersion of neurites using diffusion mri,” *NeuroImage*, vol. 133, pp. 207–223, 2016.
- [24] H. Zhang, P. L. Hubbard, G. J. Parker, and D. C. Alexander, “Axon diameter mapping in the presence of orientation dispersion with diffusion mri,” *Neuroimage*, vol. 56, no. 3, pp. 1301–1315, 2011.
- [25] B. Scherrer, A. Schwartzman, M. Taquet, M. Sahin, S. P. Prabhu, and S. K. Warfield, “Characterizing brain tissue by assessment of the distribution of anisotropic microstructural environments in diffusion-compartment imaging (diamond),” *Magnetic resonance in medicine*, vol. 76, no. 3, pp. 963–977, 2016.
- [26] D. A. Yablonskiy, G. L. Bretthorst, and J. J. Ackerman, “Statistical model for diffusion attenuated mr signal,” *Magnetic Resonance in Medicine: An Official Journal of the International Society for Magnetic Resonance in Medicine*, vol. 50, no. 4, pp. 664–669, 2003.
- [27] G. Rensonnet, B. Scherrer, G. Girard, A. Jankovski, S. K. Warfield, B. Macq, J.-P. Thiran, and M. Taquet, “Towards microstructure fingerprinting: estimation of tissue properties from a dictionary of monte carlo diffusion mri simulations,” *NeuroImage*, vol. 184, pp. 964–980, 2019.
- [28] G. Rensonnet, “Generation of a dictionary of dw-mri signals from arbitrary brain microstructure configurations,” Master’s thesis, Ecole polytechnique de Louvain, Université catholique de Louvain, 2015.
- [29] A. Berger, “Quantifying microstructural brain anomalies in patients with alzheimer’s disease via diffusion magnetic resonance imaging,” Master’s thesis, Ecole polytechnique de Louvain, Université catholique de Louvain, 2020.
- [30] Q. Dessain, N. Delinte, B. Macq, and G. Rensonnet, “Fast multi-compartment microstructure fingerprinting using deep neural networks,” in *Proc. Intl. Soc. Mag. Reson. Med*, vol. 30, p. 0560, 2022.
- [31] G. Rensonnet, “In vivo diffusion magnetic resonance imaging of the white matter microstructure from dictionaries generated by monte carlo simulations: development and validation,” tech. rep., EPFL, 2019.
- [32] R. S. Fisher, C. Acevedo, A. Arzimanoglou, A. Bogacz, J. H. Cross, C. E. Elger, J. Engel Jr, L. Forsgren, J. A. French, M. Glynn, D. C. Hesdorffer, B. Lee, G. W. Mathern, S. L. Moshé, E. Perucca, I. E. Scheffer, T. Tomson, M. Watanabe, and S. Wiebe, “Ilae official report: A practical clinical definition of epilepsy,” *Epilepsia*, vol. 55, no. 4, pp. 475–482, 2014.
- [33] WHO, “Epilepsy fact sheet,” 2023.
- [34] S. Saxena and S. Li, “Defeating epilepsy: A global public health commitment,” *Epilepsia Open*, vol. 2, no. 2, pp. 153–155, 2017.
- [35] R. D. Thijs, R. Surges, T. J. O’Brien, and J. W. Sander, “Epilepsy in adults,” *The Lancet*, vol. 393, no. 10172, pp. 689–701, 2019.

- [36] K. M. Fiest, K. M. Sauro, S. Wiebe, S. B. Patten, C.-S. Kwon, J. Dykeman, T. Pringsheim, D. L. Lorenzetti, and N. Jetté, “Prevalence and incidence of epilepsy,” *Neurology*, vol. 88, no. 3, pp. 296–303, 2017.
- [37] Y. Langan, L. Nashef, and J. W. A. Sander, “Sudden unexpected death in epilepsy: a series of witnessed deaths,” *Journal of Neurology, Neurosurgery & Psychiatry*, vol. 68, no. 2, pp. 211–213, 2000.
- [38] O. Devinsky, T. Spruill, D. Thurman, and D. Friedman, “Recognizing and preventing epilepsy-related mortality,” *Neurology*, vol. 86, no. 8, pp. 779–786, 2016.
- [39] L. Nashef, “Sudden unexpected death in epilepsy: Terminology and definitions,” *Epilepsia*, vol. 38, no. s11, pp. S6–S8, 1997.
- [40] O. Devinsky, “Sudden, unexpected death in epilepsy,” *New England Journal of Medicine*, vol. 365, no. 19, pp. 1801–1811, 2011. PMID: 22070477.
- [41] A. W. Yuen, M. R. Keezer, and J. W. Sander, “Epilepsy is a neurological and a systemic disorder,” *Epilepsy & Behavior*, vol. 78, pp. 57–61, 2018.
- [42] P. O. S. Elaine Kiriakopoulos, “Absence seizures | symptoms & risks | epilepsy foundation.” <https://www.epilepsy.com/what-is-epilepsy/seizure-types/absence-seizures>, 2019. (Accessed on 05/03/2023).
- [43] R. S. Fisher, W. v. E. Boas, W. Blume, C. Elger, P. Genton, P. Lee, and J. Engel Jr., “Epileptic seizures and epilepsy: Definitions proposed by the international league against epilepsy (ilae) and the international bureau for epilepsy (ibe),” *Epilepsia*, vol. 46, no. 4, pp. 470–472, 2005.
- [44] J. S. Duncan, J. W. Sander, S. M. Sisodiya, and M. C. Walker, “Adult epilepsy,” *The Lancet*, vol. 367, no. 9516, pp. 1087–1100, 2006.
- [45] R. S. Fisher, J. H. Cross, J. A. French, N. Higurashi, E. Hirsch, F. E. Jansen, L. Lagae, S. L. Moshé, J. Peltola, E. Roulet Perez, I. E. Scheffer, and S. M. Zuberi, “Operational classification of seizure types by the international league against epilepsy: Position paper of the ilae commission for classification and terminology,” *Epilepsia*, vol. 58, no. 4, pp. 522–530, 2017.
- [46] D. Pinault and T. J. O'brien, “Cellular and network mechanisms of genetically-determined absence seizures,” *Thalamus & related systems*, vol. 3, no. 3, pp. 181–203, 2005.
- [47] A. S. Galanopoulou, “Gabaa receptors in normal development and seizures: friends or foes?,” *Current neuropharmacology*, vol. 6, no. 1, pp. 1–20, 2008.
- [48] I. E. Scheffer, S. Berkovic, G. Capovilla, M. B. Connolly, J. French, L. Guilhoto, E. Hirsch, S. Jain, G. W. Mathern, S. L. Moshé, D. R. Nordli, E. Perucca, T. Tomson, S. Wiebe, Y.-H. Zhang, and S. M. Zuberi, “Ilae classification of the epilepsies: Position paper of the ilae commission for classification and terminology,” *Epilepsia*, vol. 58, no. 4, pp. 512–521, 2017.
- [49] S. Spencer and L. Huh, “Outcomes of epilepsy surgery in adults and children,” *The Lancet Neurology*, vol. 7, no. 6, pp. 525–537, 2008.
- [50] P. Kwan, A. Arzimanoglou, A. T. Berg, M. J. Brodie, W. Allen Hauser, G. Mathern, S. L. Moshé, E. Perucca, S. Wiebe, and J. French, “Definition of drug resistant epilepsy: Consensus proposal by the ad hoc task force of the ilae commission on therapeutic strategies,” *Epilepsia*, vol. 51, no. 6, pp. 1069–1077, 2010.
- [51] D. J. Englot, A. T. Lee, C. Tsai, C. Halabi, N. M. Barbaro, K. I. Auguste, P. A. Garcia, and E. F. Chang, “Seizure types and frequency in patients who “fail” temporal lobectomy for intractable epilepsy,” *Neurosurgery*, vol. 73, no. 5, pp. 838–844, 2013.
- [52] S. Wong, R. Mani, and S. Danish, “Comparison and selection of current implantable anti-epileptic devices,” *Neurotherapeutics*, vol. 16, pp. 369–380, 2019.
- [53] “Neuromodulation, university of florida.” <https://neurology.ufl.edu/divisions/epilepsy/neuromodulation-vns-rns-dbs/>. (Accessed on 05/02/2023).
- [54] S. E. Krahl, F. C. Martin, and A. Handforth, “Vagus nerve stimulation inhibits harmaline-induced tremor,” *Brain Research*, vol. 1011, no. 1, pp. 135–138, 2004.

- [55] S. A. Hays, R. L. Rennaker, and M. P. Kilgard, “Chapter 11 - targeting plasticity with vagus nerve stimulation to treat neurological disease,” in *Changing Brains* (M. M. Merzenich, M. Nahum, and T. M. Van Vleet, eds.), vol. 207 of *Progress in Brain Research*, pp. 275–299, Elsevier, 2013.
- [56] A. Broncel, R. Bocian, P. Klos-Wojtczak, K. Kulbat-Warycha, and J. Konopacki, “Vagal nerve stimulation as a promising tool in the improvement of cognitive disorders,” *Brain Research Bulletin*, vol. 155, pp. 37–47, 2020.
- [57] J. Beekwilder and T. Beems, “Overview of the clinical applications of vagus nerve stimulation,” *Journal of clinical neurophysiology*, vol. 27, no. 2, pp. 130–138, 2010.
- [58] J. K. Penry and J. C. Dean, “Prevention of intractable partial seizures by intermittent vagal stimulation in humans: Preliminary results,” *Epilepsia*, vol. 31, no. s2, pp. S40–S43, 1990.
- [59] D. J. Englot, J. D. Rolston, C. W. Wright, K. H. Hassnain, and E. F. Chang, “Rates and predictors of seizure freedom with vagus nerve stimulation for intractable epilepsy,” *Neurosurgery*, vol. 79, no. 3, pp. 345–353, 2016.
- [60] G. M. Ibrahim, P. Sharma, A. Hyslop, M. R. Guillen, B. R. Morgan, S. Wong, T. J. Abel, L. Elkaim, I. Cajigas, A. H. Shah, A. Fallah, A. G. Weil, N. Altman, B. Bernal, S. Medina, E. Widjaja, P. Jayakar, J. Ragheb, and S. Bhatia, “Presurgical thalamocortical connectivity is associated with response to vagus nerve stimulation in children with intractable epilepsy,” *NeuroImage: Clinical*, vol. 16, pp. 634–642, 2017.
- [61] J. L. Ardell and W. C. Randall, “Selective vagal innervation of sinoatrial and atrioventricular nodes in canine heart,” *American Journal of Physiology-Heart and Circulatory Physiology*, vol. 251, no. 4, pp. H764–H773, 1986.
- [62] E. Ben-Menachem, “Vagus nerve stimulation, side effects, and long-term safety,” *Journal of clinical neurophysiology*, vol. 18, no. 5, pp. 415–418, 2001.
- [63] “Mayo clinic vagus nerve stimulation.” <https://www.mayoclinic.org/tests-procedures/vagus-nerve-stimulation/about/pac-20384565>. (Accessed on 05/02/2023).
- [64] B. Bonaz, V. Sinniger, and S. Pellissier, “The vagus nerve in the neuro-immune axis: Implications in the pathology of the gastrointestinal tract,” *Frontiers in Immunology*, vol. 8, 2017.
- [65] L. D. Hachem, S. M. Wong, and G. M. Ibrahim, “The vagus afferent network: emerging role in translational connectomics,” *Neurosurgical Focus FOC*, vol. 45, no. 3, p. E2, 2018.
- [66] J. A. Ricardo and E. Tongju Koh, “Anatomical evidence of direct projections from the nucleus of the solitary tract to the hypothalamus, amygdala, and other forebrain structures in the rat,” *Brain Research*, vol. 153, no. 1, pp. 1–26, 1978.
- [67] B. R. Walker, A. Easton, and K. Gale, “Regulation of limbic motor seizures by gaba and glutamate transmission in nucleus tractus solitarius,” *Epilepsia*, vol. 40, no. 8, pp. 1051–1057, 1999.
- [68] K. Campbell, “Medical and science illustration, animations and communications.”
- [69] G. Aghajanian, J. Cedarbaum, and R. Wang, “Evidence for norepinephrine-mediated collateral inhibition of locus coeruleus neurons,” *Brain Research*, vol. 136, no. 3, pp. 570–577, 1977.
- [70] A. Berger, S. Vespa, L. Dricot, M. Dumoulin, E. Iachim, P. Doguet, G. Vandewalle, and R. El Tahry, “How is the norepinephrine system involved in the antiepileptic effects of vagus nerve stimulation?,” *Frontiers in Neuroscience*, vol. 15, 2021.
- [71] O. Sporns, “Structure and function of complex brain networks,” *Dialogues in clinical neuroscience*, 2022.
- [72] S. T. Grafton and L. J. Volz, “Chapter 13 - from ideas to action: The prefrontal-premotor connections that shape motor behavior,” in *The Frontal Lobes* (M. D’Esposito and J. H. Grafman, eds.), vol. 163 of *Handbook of Clinical Neurology*, pp. 237–255, Elsevier, 2019.
- [73] J. Cabral, M. L. Kringselbach, and G. Deco, “Functional connectivity dynamically evolves on multiple time-scales over a static structural connectome: Models and mechanisms,” *NeuroImage*, vol. 160, pp. 84–96, 2017. Functional Architecture of the Brain.

- [74] J. Narayanan, R. Watts, N. Haddad, D. Labar, P. Li, and C. Filippi, “Cerebral activation during vagus nerve stimulation: A functional mr study,” *Epilepsia*, vol. 43, no. 12, pp. 1509–1514, 2002.
- [75] K. Mithani, M. Mikhail, B. R. Morgan, S. Wong, A. G. Weil, S. Deschenes, S. Wang, B. Bernal, M. R. Guillen, A. Ochi, H. Otsubo, I. Yau, W. Lo, E. Pang, S. Holowka, O. C. Snead, E. Donner, J. T. Rutka, C. Go, E. Widjaja, and G. M. Ibrahim, “Connectomic profiling identifies responders to vagus nerve stimulation,” *Annals of Neurology*, vol. 86, no. 5, pp. 743–753, 2019.
- [76] K. Mithani, S. M. Wong, M. Mikhail, H. Pourmotabbed, E. Pang, R. Sharma, I. Yau, A. Ochi, H. Otsubo, O. C. Snead, E. Donner, C. Go, E. Widjaja, A. Babajani-Feremi, and G. M. Ibrahim, “Somatosensory evoked fields predict response to vagus nerve stimulation,” *NeuroImage: Clinical*, vol. 26, p. 102205, 2020.
- [77] E. Frangos and B. R. Komisaruk, “Access to vagal projections via cutaneous electrical stimulation of the neck: fmri evidence in healthy humans,” *Brain stimulation*, vol. 10, no. 1, pp. 19–27, 2017.
- [78] P.-C. Fan, S. S.-F. Peng, R.-F. Yen, J.-Y. Shieh, and M.-F. Kuo, “Neuroimaging and electroencephalographic changes after vagus nerve stimulation in a boy with medically intractable myoclonic astatic epilepsy,” *Journal of the Formosan Medical Association*, vol. 113, no. 4, pp. 258–263, 2014.
- [79] R. M. Beckstead, J. R. Morse, and R. Norgren, “The nucleus of the solitary tract in the monkey: Projections to the thalamus and brain stem nuclei,” *Journal of Comparative Neurology*, vol. 190, no. 2, pp. 259–282, 1980.
- [80] S. Standring, H. Ellis, J. Healy, D. Johnson, A. Williams, P. Collins, and C. Wigley, “Gray’s anatomy: the anatomical basis of clinical practice,” *American journal of neuroradiology*, vol. 26, no. 10, p. 2703, 2005.
- [81] A. A. Gordana Sendić, “Fornix of the brain: Anatomy and functions | kenhub.” <https://www.kenhub.com/en/library/anatomy/fornix-of-the-brain>, 2022. (Accessed on 05/02/2023).
- [82] B. Dudás, “Part i - morphology of the human hypothalamus: Anatomy, blood supply, nuclei and pathways,” in *Atlas of the Human Hypothalamus* (B. Dudás, ed.), pp. 1–24, Academic Press, 2021.
- [83] A. Alahmari, “Neuroimaging role in mental illnesses,” 04 2021.
- [84] N. Makris, D. N. Kennedy, S. McInerney, A. G. Sorensen, R. Wang, J. Caviness, Verne S., and D. N. Pandya, “Segmentation of Subcomponents within the Superior Longitudinal Fascicle in Humans: A Quantitative, In Vivo, DT-MRI Study,” *Cerebral Cortex*, vol. 15, pp. 854–869, 12 2004.
- [85] D. J. Sobotta, *Sobotta’s Atlast and Textbook of Human Anatomy*. 1908.

UNIVERSITÉ CATHOLIQUE DE LOUVAIN
École polytechnique de Louvain

Rue Archimède, 1 bte L6.11.01, 1348 Louvain-la-Neuve, Belgique | www.uclouvain.be/epl